



# Total chemocatalytic cascade conversion of lignocellulosic biomass into biochemicals

Jaeyong Park<sup>a</sup>, Umair Mushtaq<sup>b</sup>, Junjung Rohmat Sugiarto<sup>c</sup>, Deepak Verma<sup>a,b</sup>, Jaehoon Kim<sup>a,b,c,\*</sup>

<sup>a</sup> School of Mechanical Engineering, Sungkyunkwan University, 2066 Seobu-ro, Jangan-gu, Suwon, Gyeonggi-do 16419, Republic of Korea

<sup>b</sup> School of Chemical Engineering, Sungkyunkwan University, 2066 Seobu-ro, Jangan-gu, Suwon, Gyeonggi-do 16419, Republic of Korea

<sup>c</sup> SKKU Advanced Institute of Nano Technology (SAINT), Sungkyunkwan University, 2066, Seobu-ro, Jangan-gu, Suwon, Gyeonggi-do 16419, Republic of Korea

## ARTICLE INFO

### Keywords:

Lignocellulosic biomass fractionation  
Atomically dispersed catalyst  
Aromatic monomers  
Polyols  
Carboxylic acids

## ABSTRACT

Because of its complexity, selective conversion of lignocellulosic biomass into platform chemicals presents significant challenges. Herein, we converted birch wood into high-yield lignin-derived phenolic monomers and dimers and holocellulose-derived polyols and monocarboxylic acids via a two-step cascade reaction using 0.1 wt % Pd on N-doped carbon (Pd<sub>0.1</sub>/CN<sub>x</sub>) and passivated alumina-coated Ni on activated carbon (Ni<sub>2</sub>@Al<sub>2</sub>O<sub>3</sub>/AC) catalysts. The catalytic fractionation of birch sawdust using Pd<sub>0.1</sub>/CN<sub>x</sub> produced 11.1 wt% monomers, 5.6% dimers, and 63.4 wt% pulp-rich solid (PRS) based on feed weight. The subsequent conversion of PRS over passivated Ni<sub>2</sub>@Al<sub>2</sub>O<sub>3</sub>/AC produced 21.6 wt% C<sub>2</sub>–C<sub>6</sub> polyols and 7.9 wt% monocarboxylic acids. After the whole biomass conversion reaction, the Pd<sub>0.1</sub>/CN<sub>x</sub> and Ni<sub>2</sub>@Al<sub>2</sub>O<sub>3</sub>/AC catalysts were separated using their different magnetic responses and reused three times without activity loss. The structure–performance relationships of the Pd<sub>0.1</sub>/CN<sub>x</sub> catalysts synthesized using different methods and effect of passivation on the performance of the Ni<sub>2</sub>@Al<sub>2</sub>O<sub>3</sub>/AC catalyst were analyzed.

## 1. Introduction

Lignocellulosic biomass is a promising renewable and sustainable alternative to fossil resources in the fuel and chemical industries because of its abundance, affordability, and widespread availability [1,2]. Lignocellulosic biomass primarily consists of three polymeric constituents: cellulose (40–50 wt%), hemicellulose (25–35 wt%), and lignin (10–30 wt%) [3]. Fast pyrolysis and hydrothermal liquefaction are promising methods for producing bio-oil at an industrial scale; furthermore, bio-oil can be upgraded to liquid transportation fuels via catalytic hydrodeoxygenation [4]. However, producing liquid fuels and value-added platform chemicals via fast pyrolysis/hydrothermal reactions followed by catalytic upgrading is challenging because of the complex composition of bio-oil, significant catalyst coking, high H<sub>2</sub> consumption, and harsh reaction conditions. Cellulosic bioethanol production, which is another promising method of valorization lignocellulosic biomass, involves four consecutive steps, viz. pretreatment of biomass, separation of cellulose from lignin, hydrolysis of cellulose to

glucose, and fermentation of glucose to ethanol. To date, researchers have primarily focused their efforts on cellulose recovery, and the isolated lignin has been considered a byproduct [5]. Owing to the recalcitrant nature of the isolated lignin, it has been difficult to use it to produce selected aromatic chemicals and liquid fuels under mild reaction conditions [5,6]. In addition, because of its high susceptibility, hemicellulose tends to decompose uncontrollably during pretreatment [7]. Considering the high hemicellulose and lignin contents of lignocellulosic biomass, designing a method that can utilize each constituent of lignocellulosic biomass in a controllable way is promising for developing cost-effective lignocellulose biomass refineries.

To mitigate the shortcomings associated with the complex and multistep running mode and to overcome the difficulty in utilizing the constituents of whole lignocellulosic biomass, one-pot conversion reactions of lignocellulosic biomass over multifunctional catalysts have been developed. For example, gasoline-fraction fuels (e.g., C<sub>5</sub>–C<sub>6</sub> n-alkanes and branched (cyclo)alkanes [8–10]) and chemicals (e.g., diols [11], alcohols [9,12], and phenolic derivatives [9,11]) were synthesized

\* Correspondence to: School of Mechanical Engineering, School of Chemical Engineering, SKKU Advanced Institute of Nano Technology (SAINT), Sungkyunkwan University, 2066 Seobu-ro, Jangan-gu, Suwon, Gyeonggi-do 16419, Republic of Korea.

E-mail address: [jaehoonkim@skku.edu](mailto:jaehoonkim@skku.edu) (J. Kim).

<https://doi.org/10.1016/j.apcatb.2022.121280>

Received 19 December 2021; Received in revised form 21 February 2022; Accepted 2 March 2022

Available online 7 March 2022

0926-3373/© 2022 Elsevier B.V. All rights reserved.

over heterogeneous catalysts with both metallic and acid sites. However, because of the complex nature of lignocellulosic biomass, it is challenging to produce high-yield fuels and chemicals using one-pot conversion reactions.

Recently, a new lignocellulosic biomass fractionation method, termed reductive catalytic fractionation (RCF), has been developed [5, 13,14]. In contrast to typical lignocellulose biomass treatment approaches that focus on recovering pure cellulose with producing highly recalcitrant technical lignin that is enriched with C–C bond, the RCF focuses on the recovering aromatic monomers and dimers that are derived from native lignin and cellulose-rich pulp [14]. During a typical RCF process, lignin is separated from the holocellulose pulp via solvolysis, and the decomposed lignin fractions are stabilized via hydrogenation over metallic catalysts. Depending on the catalyst and fractionation conditions, researchers achieved almost theoretical yields of aromatic monomers which can be derived from lignin through the cleavage of the aryl ether  $\beta$ -O–4 bonds of pristine lignin [15,16]. However, most of the previously reported RCF studies have used catalysts with high metal loadings, such as 5 wt% Pd, 20 wt% Ni, and 5 wt% Ru [5,13,14]. In addition, to date, the research efforts to develop an efficient catalytic method for the conversion of the pulp-rich solid (PRS) collected after RCF into selected value-added platform chemicals have been scarce. The previous works are summarized in Table S1. For example, the solid fraction was used as feedstock for producing ethanol [17] and gasoline-range alkanes ( $C_4$ – $C_{12}$ ) [18,19]. To develop economically viable biorefineries, it is highly desirable to use low-metal-loaded or single-atom catalysts with high atomic efficiency for RCF and produce high-value-added platform chemicals from the PRS.

Herein, we converted whole lignocellulosic biomass into high-yield phenolic monomers, polyols, and monocarboxylic acids via a two-step cascade chemocatalytic reaction. During the first step, lignocellulosic biomass was fractionated into phenolic monomer-rich oil and PRS over a 0.1 wt% Pd on N-doped carbon ( $Pd_{0.1}/CN_x$ ) catalyst. During the second step, the PRS embedded with  $Pd_{0.1}/CN_x$  was converted into polyols and monocarboxylic acid over an alumina-coated Ni on activated carbon ( $Ni_2@Al_2O_3/AC$ ) catalyst. Subsequently, the  $Pd_{0.1}/CN_x$  and  $Ni_2@Al_2O_3/AC$  catalysts were magnetically separated and reused to demonstrate their high recyclability. Furthermore, the properties of the catalysts, RCF performance of the  $Pd_{0.1}/CN_x$  catalysts prepared using different synthesis methods, RCF optimization, proposed reaction pathways for obtaining polyols and monocarboxylic acids, and recyclability of the catalysts were analyzed.

## 2. Experimental

### 2.1. Catalyst preparation

The  $CN_x$  was synthesized by the calcination of a mixture of 1.24 g of melamine (99% purity, Sigma–Aldrich, USA), 1.36 g of terephthalaldehyde (98% purity, Alfa Aesar, USA), and ground 5 g of potassium hydroxide (KOH; >85% purity, pellets, Daejung Chemicals and Metals, South Korea) [20]. The calcination conditions were 250 °C for 3 h, and then at 800 °C for 1 h under a  $N_2$  flow of 100 mL  $min^{-1}$ . After the calcination, the synthesized  $CN_x$  powders were rinsed with distilled and deionized (DDI) water (EXL7-A16 pure and ultrapure water system, Vivagen, South Korea) until the pH of the filtrate reached ~6. The washed  $CN_x$  powders were then dried in a drying oven at 80 °C. Three different methods were used to load Pd on the  $CN_x$  support: wet impregnation (WI), coimpregnation (CI) with urea (ACS reagent, >99.0%, Sigma–Aldrich), and deposition–precipitation (DP) with urea. For the WI method, a desired amount of palladium(II) nitrate dihydrate ( $Pd(NO_3)_2 \cdot 2H_2O$ , Sigma–Aldrich) was dissolved in 1.5 mL of DDI water with stirring, and then 0.6 g of  $CN_x$  was added to the aqueous Pd salt solution. The slurry was subsequently stirred at 90 °C until water evaporated. The dried powder was calcinated at 300 °C for 1 h under a 5%  $H_2/Ar$  (JC Gas Company, South Korea) flow of 100 mL  $min^{-1}$ . For

the CI method, desired amounts of  $Pd(NO_3)_2 \cdot 2H_2O$  and urea (urea/Pd molar ratios of 4 and 8) were dissolved in 1.5 mL of DDI water, and then 0.6 g of  $CN_x$  was added to the Pd salt and urea solution. The solution was subsequently stirred at 90 °C until water evaporated. Thereafter, the dried powder was calcined using the same method used for the WI method. For the DP method, 0.6 g of  $CN_x$  was dispersed in 24 mL of DDI water via sonication for 30 min in a Teflon-lined autoclave. Desired amounts of  $Pd(NO_3)_2 \cdot 2H_2O$  (0.05–0.1 wt%) and urea (urea/Pd molar ratio of 4) were added to the  $CN_x$  dispersion. Thereafter, the dispersion was mixed at  $25 \pm 2$  °C for 1 h, heated to 90 °C at a ramping rate of 5 °C  $min^{-1}$ , and allowed to rest at 90 °C for 4 h. Subsequently, the Teflon-lined autoclave was opened and the slurry stirred continuously at 90 °C until water evaporated. The dried powder was calcined using the same method used for the WI method. The catalysts synthesized using the WI, CI, and DP methods are denoted as  $Pd_z/CN_x$ -WI,  $Pd_z/CN_x$ -CIy, and  $Pd_z/CN_x$ -DPy, respectively, where z and y denote the Pd loading and urea/Pd ratio, respectively.

For the synthesis of core–shell Ni–alumina on activated carbon ( $Ni_2@Al_2O_3/AC$ ), 0.1 mol of nickel(II) nitrate hexahydrate ( $Ni(NO_3)_2 \cdot 6H_2O$ , 98% purity, Alfa Aesar) and 0.05 mol of aluminum nitrate nonahydrate ( $Al(NO_3)_3 \cdot 9H_2O$ , >98.0% purity, Alfa Aesar) were dissolved in 150 mL of DDI water, and then 1.12 g of activated carbon (AC; –20 to +40 mesh, Alfa Aesar) was added to the solution; the obtained dispersion is denoted dispersion A. Thereafter, 0.27 mol of sodium hydroxide (NaOH, >98% purity, pellets, Sigma–Aldrich) and 0.1 mol of sodium carbonate ( $Na_2CO_3$ , >99.0% purity, Sigma–Aldrich) were dissolved in 150 mL of DDI water; the obtained solution is denoted solution B. Next, solution B was added dropwise to dispersion A. The mixture was aged at 80 °C for 20 h. The obtained solid was collected via centrifugation and rinsed three times with DDI water and ethanol (HPLC grade, Daejung Chemicals and Metals). Thereafter, the precipitated solid was dried in a drying oven at 80 °C overnight. The dried solid was reduced in a calcination tube at 800 °C for 6 h under a 5%  $H_2/Ar$  flow of 100 mL  $min^{-1}$ . The reduced catalyst is denoted as  $Ni_2@Al_2O_3/AC$ . For the passivation of metal sites, the  $Ni_2@Al_2O_3/AC$  catalyst was calcined in a calcination tube in the temperature range of 200–300 °C for 2–4 h at a ramping rate of 10 °C  $min^{-1}$  under a 1–21%  $O_2/N_2$  flow of 100 mL  $min^{-1}$ .

### 2.2. Catalyst characterization

An inductively plasma–mass spectrometry (ICP–MS; Agilent 7500, Agilent Technologies Inc., USA) instrument was used to determine the metal contents in the catalysts. A high-angle annular dark-field scanning transmission electron microscopy (HAADF–STEM; FEI Titan TM80–300, USA) was used to analyze the morphology and particle size of the catalysts. A STEM–energy dispersive X-ray spectroscopy (STEM–EDS; FEI Talos F200X, USA) was used to analyze the morphology and elemental mapping of the catalysts. Pd K-edge X-ray absorption spectroscopy (XAS) were obtained at the 10 C synchrotron beamline of the Pohang Accelerator Laboratory, which was operated in the fluorescence mode using a Si (111) double-crystal monochromator. Pd foil spectrum was collected for energy calibration as a reference. The Athena/Artemis software was used to process the X-ray absorption near-edge structure (XANES) and extended X-ray absorption fine structure (EXAFS) profiles. The EXAFS profiles in the R-space were obtained by Fourier-transform of the  $k^2$ -weighted profiles in the  $k$ -range of 3.0–11.0 Å<sup>−1</sup>. The phase structures of the catalysts were characterized by high-power powder X-ray diffraction (HP Powder XRD) using D8 ADVANCE (Bruker Corporation, USA) equipped with Cu K $\alpha$  radiation at 40 kV and 100 mA in the 2 $\theta$  range of from 5° to 90° with a scanning speed of 5°  $min^{-1}$ . The surface electron states of the catalysts were characterized by X-ray photoelectron spectroscopy (XPS; ESCA2000 spectrometer, Thermo Scientific, UK) measurements using a twin node X-ray source of Al K $\alpha$  (1486.6 eV) and a Mg K $\alpha$  (1253.6 eV). The acidity of the catalysts was determined through  $NH_3$  temperature-programmed desorption ( $NH_3$ -TPD) using a BELCAT-M instrument (BEL Inc., Japan) equipped with a thermal

conductivity detector (TCD) and quadrupole mass spectrometry (QMS; TRANSECTOR® CPM 3, Inficon Inc., USA) residual gas analyzer. For the NH<sub>3</sub>-TPD experiments, the Pd- and Ni-based catalysts were reduced under a 5% H<sub>2</sub>/Ar flow of 50 mL min<sup>-1</sup> at 300 and 800 °C, respectively. Thereafter, the catalysts were naturally cooled to 100 °C under a 5% H<sub>2</sub>/Ar flow of 50 mL min<sup>-1</sup>. Next, the gas flow was switched to 4.95% NH<sub>3</sub>/He, and the chamber was purged for 1 h at 100 °C to promote the adsorption of NH<sub>3</sub> at the acid sites of the catalysts. Subsequently, the gas flow was switched to He at 50 mL min<sup>-1</sup>, and the chamber was purged for 0.5 h at 100 °C to remove the residual gases and physisorbed NH<sub>3</sub>. Desorption was performed in the temperature range of 100–800 °C at a ramping rate of 5 °C min<sup>-1</sup> under a He flow of 30 mL min<sup>-1</sup>. The amount of desorbed NH<sub>3</sub> was monitored continuously using the TCD and QMS instrument.

### 2.3. Two-step cascade catalytic conversion of birch wood

For a typical RCF experiment, 3 g of birch wood (*Betula*, hardwood, 42.1 wt% glucans, 21.3 wt% xylans, 21.4 wt% lignin, 1.61 wt% moisture, <0.1 wt% ash, and 13.6 wt% other components [21]), 0.3–0.45 g of Pd<sub>0.1</sub>/CN<sub>x</sub>, and 60 mL of methanol (HPLC grade, Daejung Chemicals and Metals) were loaded into a 140-mL batch reactor. The reactor was then closed, and 10 MPa of H<sub>2</sub> or N<sub>2</sub> (99.999%, JC Gas Company) was injected for leak test. Subsequently, the O<sub>2</sub> dissolved in the liquid and other gases was removed from reactor by purging with H<sub>2</sub> or N<sub>2</sub> three times through a deep-in tubing line. Thereafter, the reactor was pressurized to 2.0–3.0 MPa using H<sub>2</sub> or a H<sub>2</sub>/N<sub>2</sub> mixture, followed by heating it to 200–250 °C at a ramping rate of ~10 °C min<sup>-1</sup>. The reactor temperature was kept for 2–3 h. After the reaction finished, the reactor was cooled down quickly under 100 °C by a water to avoid additional reaction during cooling. Next, the reactor was cooled to 25 ± 2 °C by an electric fan, and then the gas was expelled from the reactor. Subsequently, the reactor was opened, and the products which consisted of decomposed holocellulose- and lignin-derived liquid and solid was collected to a beaker by rising the reactor with water, acetone (HPLC grade, Daejung Chemicals and Metals), and ethanol. The liquid and solid mixture was separated by a polyvinylidene difluoride (PVDF, 45 μm pore size, Whatman, USA) filter, and the solid product was rinsed with 50 mL of each DDI water, ethanol, and acetone to dissolve the soluble organics and transfer them to the filtrate. The obtained solid was dried in a drying oven at 80 °C overnight. The dried solid product is denoted as PRS. The methanol, ethanol, and acetone were removed from the liquid product, which comprised a mixture of primarily lignin-derived components, small amounts of holocellulose-derived species, and solvents (methanol, water, ethanol, and acetone) at 50 °C and 0.02 MPa during 1 h by a rotary evaporator. Three cycles of liquid–liquid extraction (LLE) was used to separate the residual liquid, which contained holocellulose- and lignin-derived components and water. To collect most of the lignin-derived components, 100 mL of dichloromethane (DCM, HPLC grade, Daejung Chemicals and Metals) was added to the separatory funnel that contained the aqueous phase for each LLE cycle. After LLE, the remaining DCM in the DCM phase was removed by rotary evaporation at 50 °C and 0.04 MPa for 0.5 h and subsequently vacuum drying at 50 °C and ~0.01 MPa for 12 h. The collected product is designated as DCM-soluble organics (DSOs). The water phase was collected to an 80-mL vial and was frozen at –80 °C for at least 24 h. The frozen aqueous phase was dried using a freeze dryer (FDB-5502, Operon, South Korea) at –40 °C and ~0.01 MPa pressure for 2 d. The residual product is designated as water-soluble organics (WSOs).

The DSOs, WSOs, and PRS yields were calculated as follows:

$$\text{DSO yield (wt\%)} = \frac{\text{Weight of dried DSOs}}{\text{Weight of dry ash free wood}} \times 100\%, \quad (1)$$

$$\text{WSO yield (wt\%)} = \frac{\text{Weight of dried WSOs}}{\text{Weight of dry ash free wood}} \times 100\%, \quad (2)$$

$$\text{PRS yield (wt\%)} = \frac{\text{Weight of dried solid residue} - \text{weight of catalyst}}{\text{Weight of dried wood}} \times 100\% \quad (3)$$

For a typical conversion of the RCF pulp embedded with Pd<sub>0.1</sub>/CN<sub>x</sub>, 2.26 g of solid residue from RCF (1.81 g of PRS + 0.45 g of RCF catalyst), 1 g of Ni<sub>2</sub>@Al<sub>2</sub>O<sub>3</sub>/AC, and 40 mL of water were added to a 140-mL batch reactor. The reactor was purged and pressurized with H<sub>2</sub> using the same procedure utilized for the RCF experiment. Thereafter, the reactor was heated to 270 °C at a heating rate of ~10 °C min<sup>-1</sup>, and the reaction proceeded for 1 h. Subsequently, the reactor was cooled using the same procedure used for the RCF experiment. After cooling, the reactor pressure was recorded to calculate the quantity of gas produced. The gas phase was collected in a 0.5-L Tedlar bag through the vent line. The reactor was opened, the product was collected in an 80-mL vial, and then separated using a PVDF filter. The solid residue was rinsed with water and then dried in a vacuum oven at 75 °C under ~0.01 MPa for 12 h. The weight of the dried solid residue, which contained Pd<sub>0.1</sub>/CN<sub>x</sub> and Ni<sub>2</sub>@Al<sub>2</sub>O<sub>3</sub>/AC catalysts, partially reacted lignocellulose constituents, and coke, was recorded to calculate the PRS conversion. The dried solid residue was separated using a magnet to collect the non-magnetic (Pd<sub>0.1</sub>/CN<sub>x</sub>) and magnetic (Ni<sub>2</sub>@Al<sub>2</sub>O<sub>3</sub>/AC) catalysts, and the separated catalysts were subjected to recyclability testing. Microcrystalline cellulose (20 μm, powder, Sigma–Aldrich), glucose (ACS reagent, Sigma–Aldrich), and fructose (99%, Alfa Aesar) were converted over the Ni<sub>2</sub>@Al<sub>2</sub>O<sub>3</sub>/AC catalyst using the same procedure utilized for the PRS conversion. The PRS, microcrystalline cellulose, glucose, and fructose conversions were calculated as follows:

$$\text{Holocellulose (constituent) conversion (wt\%)} = \left( 1 - \frac{\text{Weight of dried solid residue} - \text{Weight of catalysts}}{\text{Weight of dried feedstock}} \right) \times 100\%, \quad (4)$$

### 2.4. Product characterization

The DSOs were qualitatively analyzed using a gas chromatography (GC, 7890 A Agilent Technologies Inc., USA) apparatus with a time-of-flight mass spectrometry (TOF/MS) detector and an Rxi-5Sil-MS capillary column (30 m × 0.25 mm × 0.25 μm, Restek, USA). The monomers in the DSO phase were quantitatively analyzed using a 6890 N (Agilent Technologies Inc., USA) GC instrument apparatus with a flame ionization detector (FID) and a Rxi-5Sil-MS capillary column (30 m × 0.25 mm × 0.25 μm). The detailed descriptions of qualitative and quantitative analysis of DSOs were presented [Supplementary data A](#). The structure of the DSOs was analyzed using two-dimensional heteronuclear single quantum coherence nuclear magnetic resonance (2D HSQC NMR, 700 MHz AVANCE III spectrometer, Bruker, USA) spectroscopy apparatus equipped with a 5-mm inverse-gradient cryoprobe. For NMR analysis, 100 mg of DSOs and 700 μL of deuterated dimethyl sulfoxide (99.9% purity, Cambridge Isotope Laboratories, USA) were mixed. The details of 2D HSQC NMR analysis was described in our previous paper [21]. The PRS composition was examined using thermogravimetric analysis (TGA, Q50 TGA instrument, TA Instruments, USA). The detailed descriptions of the TGA analysis was given in [Supplementary data B](#). Mixtures of hexane (HPLC grade, Daejung Chemicals and Metals) and ethyl acetate (HPLC grade, Daejung Chemicals and Metals) with different ratios of 0–60 wt% were used to fractionate the monomer, dimer, and trimer fractions of the DSOs [22]. A gel permeation chromatography (GPC, Agilent 1100 Series, Agilent Technologies Inc., USA) apparatus equipped with a PLgel 10 μm MIXED-B column (300 mm × 7.5 ID; Agilent Technologies Inc., USA) and a refractive index (RI) detector was performed to analyze the molecular weight distribution of the fractionated DSOs was analyzed using. The liquid sample was analyzed using tetrahydrofuran with a flow rate of 1 mL min<sup>-1</sup> as the mobile phase. Polystyrene standards were used to calibrate the molecular weights.

The holocellulose-derived species produced from the PRS (or microcrystalline cellulose) were qualitatively analyzed using GC–TOF/MS with or without trimethylsilylation. For the GC–TOF/MS analysis without trimethylsilylation, the liquid sample, which contained decomposed holocellulose and water, was dried using a freeze dryer. Thereafter, 0.1 g of freeze-dried sample was dissolved in 1 mL of methanol and analyzed via GC–TOF/MS under the same conditions used for the analysis of the DSOs. For the GC–TOF/MS analysis with trimethylsilylation, the freeze-dried sample was dissolved in 0.5 mL of acetonitrile (ACN, HPLC grade, Daejung Chemicals and Metals) and 0.5 mL of *N*-methyl-*N*-(trimethylsilyl)trifluoroacetamide (MTFA, 97% purity, Alfa Aesar). Subsequently, the solution was heated to 80 °C for 0.5 h, followed by GC–TOF/MS analysis under the same conditions used for the analysis of the DSOs. The holocellulose-decomposed species obtained from the PRS (or microcrystalline cellulose) were qualitatively analyzed using a Waters e2695 HPLC separation module (Waters Alliance, USA) equipped with an Aminex HPX-87 H column (300 mm × 7.8 mm ID; Bio-Rad, USA) and an RI detector. Each liquid sample was analyzed at least twice using 0.005 M aqueous sulfuric acid ( $\text{H}_2\text{SO}_4$ , ≥99.5%, Sigma–Aldrich) and a mixture of 5% ACN and 0.005 M aqueous  $\text{H}_2\text{SO}_4$  at a flow rate of 0.4 mL min<sup>−1</sup> as the mobile phases. The temperature of the column and RI detector was maintained at 50 °C. The molecular weight distributions of the holocellulose-decomposed products were analyzed using gel filtration chromatography (GFC) utilizing a Waters e2695 HPLC separation module (Waters Alliance, USA) equipped with a TSKgel G5000PW<sub>XL</sub> column (300 mm × 7.8 mm ID; TOSOH, Japan). Each liquid sample was analyzed using water with a flow rate of 0.5 mL min<sup>−1</sup> as the mobile phase. The compositions of the gaseous products collected from the PRS (or microcrystalline cellulose) reaction were analyzed using a PerkinElmer Clarus 600 GC-Model Arnel 1115PPC refinery gas analyzer (RGA; PerkinElmer, USA) equipped with an FID and a TCD. The temperatures of the oven, FID, and TCD were set to 60, 250, and 200 °C, respectively. Detailed information on the RGA–GC experiments are included in our previous paper [23].

### 3. Results and discussion

#### 3.1. Total chemocatalytic conversion of lignocellulosic biomass into biochemicals

The Sankey diagram of the chemocatalytic two-step cascade conversion of lignocellulosic biomass including the material balance is presented in Fig. 1. First, the dried birch wood was subjected to RCF in methanol over  $\text{Pd}_{0.1}/\text{CN}_x$ . Thereafter, the delignified PRS and liquid product, which primarily comprised aromatic species, such as LDPMs, lignin-derived dimers (LDDs) and lignin-derived oligomers (LDOs), and a small fraction of glucan- and xylan-decomposed species, were collected. Subsequently, the LDPMs, LDDs, and LDOs were separated from the glucan- and xylan-decomposed species via LLE with DCM and water. The LDPM, LDD, and LDO yields based on the total weight of glucans, xyans, and lignin, were 11.1 wt%, 5.6%, and 3.3 wt%, respectively. The LDPM, LDD, and LDO fractions of the DSOs were separated via LLE using hexane and ethyl acetate mixtures with varying hexane-to-ethyl acetate weight ratios (Fig. S1). The LDPM fraction can be used to produce bulk and fine chemicals such as, phenol [1,24], ethylbenzene [25], terephthalic acid [26], indanes [27], aromatic amines [19], and cyclohexanone [28], and other types of platform chemicals [29]. Alternatively, the LDPM and LDD fractions can be subsequently hydrogenated to produce bio-gasoline and bio-jet fuel (Fig. S2). Conversely, the LDO fraction can be used as raw material to manufacture resin-based ink-vanish [1] and rigid polyurethane foam [30], to produce bio-ship fuel via mild hydroprocessing or supply heat and power in biorefineries. Moreover, the whole-lignin-derived oil can be hydrodeoxygenated to produce high-energy-density drop-in biofuel [31]. The WSO fraction (6.4 wt%) consisted of C5 sugars and methylated C5 sugars, such as ribofuranose and methyl xylopyranoside, as the primary products, and methylated C6 sugars, such as methyl 6-deoxy-galactopyranoside and methyl galactose, as the secondary products (Fig. S3). The methylated C5 and C6 sugars were generated via the condensation reaction between decomposed sugars and methanol during the RCF. The WSO fraction can be subsequently hydrodeoxygenated

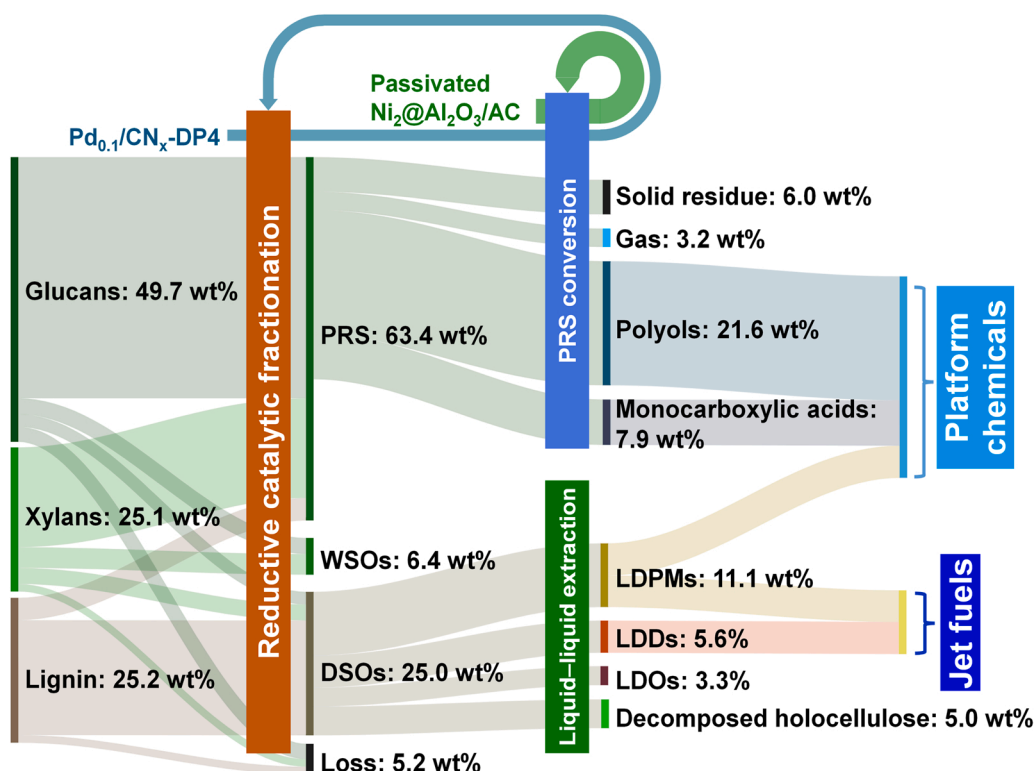


**Fig. 1.** Sankey diagram of the total cascade conversion of birch wood based on the weight of glucans + xyans + lignin. PRS, WSOs, and DSOs denote the pulp-rich solid, water-soluble organics, and dichloromethane-soluble organics, respectively, produced via reductive catalytic fractionation of birch wood. LDPMs, LDDs and LDOs denote lignin-derived phenolic monomers, lignin-derived dimers and lignin-derived oligomers, respectively.  $\text{Pd}_{0.1}/\text{CN}_x\text{-DP4}$  and  $\text{Ni}_2 @\text{Al}_2\text{O}_3/\text{AC}$  denote 0.1 wt% Pd on N-doped carbon synthesized via deposition–precipitation using urea (urea/Pd molar ratio = 4) and Ni–alumina core–shell catalyst on activated carbon (Ni/Al molar ratio = 2).



to produce biofuels [19].

The primary constituents of the PRS were glucans and xylans with recovery yields of 42.0 and 17.4 wt%, respectively. Typically, the powder-type catalysts used for RCF are embedded into the PRS matrix (Fig. S4). The addition of a pelletized catalyst to a screen bed installed inside a batch reactor can produce catalyst-free PRS. However, the fractionation efficiency in terms of lignin oil and LDPM yields of this method is lower than that of the fractionation reaction performed in the absence of a catalyst screen bed [17]; This was ascribed to the solid–solid contact in the presence of the screen bed being less effective than that in the absence of the screen bed. The conversion of PRS over the pre-embedded Pd<sub>0.1</sub>/CN<sub>x</sub> catalyst did not generate selective products, as discussed in Section 3.5. Therefore, it is desirable to develop a new type of catalyst for the selective conversion of PRS into value-added biochemicals. Herein, we used a passivated Ni<sub>2</sub>@Al<sub>2</sub>O<sub>3</sub>/AC catalyst with metallic and acid sites to produce highly selective polyols, such as EG, 1, 2-PG, and 1,2-BG, with a yield of 21.6 wt%, and monocarboxylic acids, such as AA, PA, and BA, with a yield of 7.9 wt%. The market sizes for EG and 1,2-PG (23 and 1.8 million tons per year in 2015 [32], respectively) are large, and their corresponding prices are 1000 [33] and 1450 USD/ton [34], respectively. Currently, EG and 1,2-PG are used as polyester monomers, heat-transfer agents, antifreeze agents, as well as solvents, surfactants, and ingredients in the food and pharmaceutical industries [32]. The market sizes of AA, PA, and BA were 16, 0.38, and 0.5 million tons per year, respectively, between 2011 and 2015, and their corresponding prices ranged between 500 and 850 USD/ton, 1600 and 2300 USD/ton, and 1800 and 1900 USD/ton, respectively [35]. AA can be used to synthesize vinyl acetate, cellulose acetate, alkyl acetates, and acetic anhydride [36]. PA can be used to fabricate antifungal agents and cellulose acetate propionate and as solvent for resins and paints [37]. BA can be used to produce cellulose acetate butyrate, butyrate

esters, and methyl butyrate, which are used in the food and cosmetic industries [38]. Based on their carbon balances, the carbon yields of polyols, carboxylic acids, LDPMs, and LDDs were 19.4, 7.8, 17.6 and 5.3 C%, respectively (Fig. S5), indicating that 40.5 C% of holocellulose and 69.8 C% of lignin were converted into platform chemicals. Therefore, whole lignocellulosic biomass was converted into value-added platform chemicals via highly chemoselective two-step cascade conversion over the Pd<sub>0.1</sub>/CN<sub>x</sub> and passivated Ni<sub>2</sub>@Al<sub>2</sub>O<sub>3</sub>/AC catalysts.

### 3.2. RCF performance over the Pd<sub>0.1</sub>/CN<sub>x</sub> catalysts

Most of the previous studies on RCF used high-metal-loaded catalysts (e.g., 5 wt% Pd [39], 5 wt% Ru [15], 1–5 wt% Pt [40], and 10–21 wt% Ni [16,17]). Considering the high cost of noble metals, the development of catalysts with lower metal loadings can be economically viable. The use of catalysts with low Pd loadings has been explored previously. For example, the RCF of birch wood using a 0.25 wt% Pd on CN<sub>x</sub> catalyst prepared using an impregnation method presented a PRS yield of 63.4 wt%, LDPMs yield of 52.7 C%, and a degree of delignification (DOD) of 87.1 wt% [21]. However, the RCF performance deteriorated upon decreasing the Pd loading of the catalyst to 0.1 wt% (PRS yield of 61.3 wt%, LDPM yield of 45.3 C%, and DOD of 72.5%). In this study, to examine the possibility of decreasing the metal loading of the catalyst and gain insight into the relationship between the Pd particle size and RCF performance, 0.1 wt% Pd loaded on CN<sub>x</sub> catalysts were prepared via the WI, CI, and DP methods. The RCF result using the Pd<sub>0.1</sub>/CN<sub>x</sub>-DP4 catalyst is summarized in Table 1. The PRS, DSO and WSO yields were 60.3, 24.7, and 9.77 wt%, respectively. The LDPMs yield was 53.6 C%, which was the maximum theoretical yield of aromatic monomers that can be achieved using birch wood [15,39]. Additionally, the DOD produced using the Pd<sub>0.1</sub>/CN<sub>x</sub>-DP4 catalyst was high (84.6 wt%). The

**Table 1**  
Reductive catalytic fractionation of birch wood over Pd-based catalysts.<sup>a</sup>

Entry	Catalyst	Product yield <sup>b</sup> (wt%)			LDPM carbon yield <sup>c</sup> (C%)								Retention of wood constituents in PRS <sup>d</sup> (wt %)		DOD <sup>e</sup> (wt%)	STY <sup>f</sup> (g g <sup>-1</sup> h <sup>-1</sup> )
		PRS	DSO	WSO	P-G (1)	P = G (2)	POH-G (3)	P-S (4)	P=S (5)	POH-S (6)	Others	Total	Holocellulose	Lignin		
1	Blank	63.7	17.6	7.36	0.18	0.87	0.33	0.10	1.24	2.43	7.75	12.9	73.9	53.0	47.0	N.A. <sup>g</sup>
2	CN <sub>x</sub>	67.4	16.6	5.32	0.78	2.96	0.59	2.46	5.64	0.62	12.1	25.1	78.0	49.9	50.1	N.A.
3 <sup>h</sup>	Pd <sub>0.1</sub> /CN <sub>x</sub> -DP4	60.3	24.7	9.77	11.6	N.D.	0.96	32.6	0.53	1.82	6.12	53.6	79.6 <sup>i</sup>	15.4	84.6	1186.6
4 <sup>j</sup>	Pd <sub>5</sub> /AC-0.015	56.5	26.7	8.21	0.79	N.D. <sup>k</sup>	12.0	2.44	N.D.	29.2	7.11	50.6	72.7	9.1	90.9	224.7
5 <sup>h</sup>	Pd <sub>0.1</sub> /CN <sub>x</sub> -WI	59.3	24.0	5.34	10.1	N.D.	2.16	23.1	0.07	5.84	5.41	46.8	75.0	24.2	75.8	1078.6
6 <sup>h</sup>	Pd <sub>0.1</sub> /CN <sub>x</sub> -CI4	59.6	24.3	6.91	5.81	N.D.	1.32	28.5	0.46	3.20	5.62	45.0	76.9	22.1	77.9	1000.9
7 <sup>h</sup>	Pd <sub>0.1</sub> /CN <sub>x</sub> -CI8	60.3	24.3	5.53	11.6	N.D.	0.96	26.3	0.19	6.54	5.88	51.4	79.3	16.0	84.0	1151.2

<sup>a</sup> Pd<sub>5</sub>/AC and Pd<sub>0.1</sub>/CN<sub>x</sub> designate 5 wt% Pd on activated carbon and 0.1 wt% Pd on N-doped carbon, respectively. WI, CI, and DP denote wet impregnation, coimpregnation with urea (urea/metal ratio = y) and deposition–precipitation with urea (urea/metal ratio = y), respectively. PRS, pulp-rich solid; DSO, dichloromethane-soluble organics; WSO, water-soluble organics; LDPM, lignin-derived phenolic monomer; DOD, degree of delignification

<sup>b</sup> Based on dried ash-free birch wood.

<sup>c</sup> Based on the carbon content of lignin in birch wood. The detailed procedure of the LDPM carbon yield calculation is included in Supplementary data A. The detailed LDPMs compositions are listed in Table S2. P-G, P = G, POH-G, P-S, P=S, and POH-S designate 4-*n*-propyl guaiacol, 4-*n*-propenyl guaiacol, 4-*n*-propanol guaiacol, 4-*n*-propyl syringol, 4-*n*-propenyl syringol, and 4-*n*-propanol syringol, respectively.

<sup>d</sup> The weights of glucose and xylose in birch wood were used to calculate the holocellulose retention, and the weight of lignin in birch wood was used to calculate the lignin retention. The weights of glucose, xylose, and lignin in birch wood were determined using the Klason method. The weights of holocellulose, and lignin in the PRS were determined using thermogravimetric analysis, as described in Supplementary data B.

<sup>e</sup> Based on the weight of lignin in birch wood, which was determined using the Klason method.

<sup>f</sup> Space time yield (STY) =  $\frac{\text{weight of LDPM (g)}}{\text{weight of metal in catalysts (g)} \times \text{reaction time (h)}}$

<sup>g</sup> N.A., Not available

<sup>h</sup> Reaction conditions: 3 g of birch wood, 0.45 g of catalyst, 60 mL of methanol, initial H<sub>2</sub> pressure of 3.0 MPa, 250 °C, 3 h.

<sup>i</sup> The composition of holocellulose (70.7% glucans and 29.3% xylans) was determined using the Klason method.

<sup>j</sup> Reaction conditions: 3 g of birch wood, 0.045 g of catalyst, 60 mL of methanol, initial H<sub>2</sub> pressure of 3.0 MPa, 250 °C, 3 h.

<sup>k</sup> N.D., Not detected

LDPMs yield and DOD in the absence of a catalyst or in the presence of the  $\text{CN}_x$  support were significantly lower than those using the  $\text{Pd}_{0.1}/\text{CN}_x\text{-DP4}$  catalyst, indicating the role of Pd sites in the stabilization of the decomposed lignin intermediates. Previous studies using catalyst-to-feed ratios of 0.15–0.0075 have demonstrated that the RCF of birch using commercially available 5 wt% Pd on activated carbon ( $\text{Pd}_5/\text{AC}$ , Sigma–Aldrich) catalysts presented high LDPM yields ( $\sim 50$  C %) and high DODs [21,39,41,42]. The good RCF performance of the 0.1 wt% Pd-loaded catalyst prompted us to reevaluate the RCF performance of the  $\text{Pd}_5/\text{AC}$  catalyst and determine the lowest catalyst-to-feed ratio (Fig. S6). The PRS, DSO, and WSO yields were  $\sim 55$ ,  $\sim 27$  and  $\sim 7$  wt%, respectively, in the catalyst-to-feed ratios from 0.0075 to 0.1. High LDPM yields ( $>50$  C %) were achieved at catalyst-to-feed ratios  $\geq 0.015$ . The highest space-time yield (STY) of  $224.7 \text{ g}_{\text{LDPMs}} \text{ g}_{\text{Pd}}^{-1} \text{ h}^{-1}$

was achieved over the  $\text{Pd}_5/\text{AC}$  catalyst at the lowest catalyst-to-feed ratio (0.015) associated with a high RCF performance. This STY value was approximately five times lower than that achieved over the  $\text{Pd}_{0.1}/\text{CN}_x\text{-DP4}$  catalyst ( $1186.6 \text{ g}_{\text{LDPMs}} \text{ g}_{\text{Pd}}^{-1} \text{ h}^{-1}$ ). In summary, high LDPM yields, DODs, and STYs can be achieved using 0.1 wt% Pd-loaded catalysts. The RCF was optimized by varying reaction conditions over the  $\text{Pd}/\text{CN}_x\text{-DP4}$  catalyst, as presented in Figs. S7–11 and discussed in Supplementary data C. Under the optimal RCF conditions, the PRS, holocellulose retention, DOD, and DSO and LDPM yields were 60.3 wt%, 79.6 wt%, 84.6 wt%, 24.7 wt%, and 53.6 C% respectively. The LDPM yield comprised 11.6 C% of P–G, 0.96 C% of POH–G, 32.6 C% of P–S, 0.53 C% of 4-*n*-propenyl syringol, and 1.82 C% of POH–S.

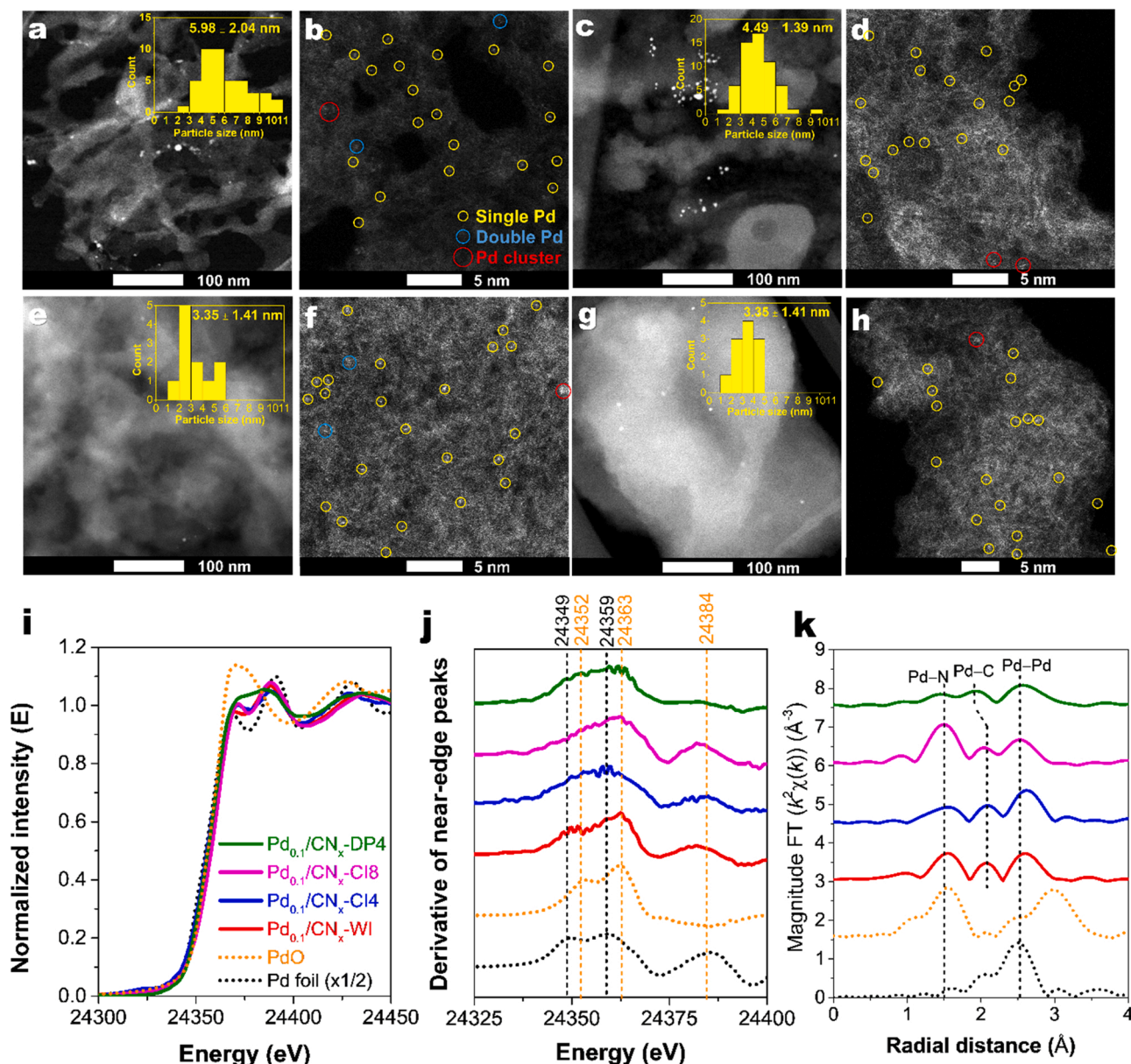


**Fig. 2.** High-angle annular dark-field scanning transmission electron microscopy images of (a) and (b)  $\text{Pd}_{0.1}/\text{CN}_x\text{-WI}$ , (c) and (d)  $\text{Pd}_{0.1}/\text{CN}_x\text{-CI4}$ , (e) and (f)  $\text{Pd}_{0.1}/\text{CN}_x\text{-CI8}$ , and (g) and (h)  $\text{Pd}_{0.1}/\text{CN}_x\text{-DP4}$ . The average particle sizes of  $\text{Pd}_{0.1}/\text{CN}_x\text{-WI}$ ,  $\text{Pd}_{0.1}/\text{CN}_x\text{-CI4}$ ,  $\text{Pd}_{0.1}/\text{CN}_x\text{-CI8}$ , and  $\text{Pd}_{0.1}/\text{CN}_x\text{-DP4}$  were  $5.98 \pm 2.04$ ,  $4.49 \pm 1.39$ ,  $3.35 \pm 1.41$ , and  $3.44 \pm 1.11$  nm, respectively. (i) X-ray absorption near-edge structure (XANES) profiles, (j) first derivatives of the XANES profiles, and (k) extended X-ray absorption fine structure profiles of Pd foil, PdO,  $\text{Pd}_{0.1}/\text{CN}_x\text{-WI}$ ,  $\text{Pd}_{0.1}/\text{CN}_x\text{-CI4}$ ,  $\text{Pd}_{0.1}/\text{CN}_x\text{-CI8}$  and  $\text{Pd}_{0.1}/\text{CN}_x\text{-DP4}$  (k-range of 3.0–11.0 Å<sup>-1</sup> and Rbkg of 1.2). The coordination numbers (CNs) and atomic distance (R) fitting results are listed in Table S4.  $\text{Pd}_{0.1}/\text{CN}_x$  denotes 0.1 wt% Pd loaded on N-doped carbon, and WI, CIy, and DPy denote wet impregnation, coimpregnation with urea (urea/metal ratio = y), and deposition–precipitation with urea (urea/metal ratio = y), respectively.

### 3.3. Structure–RCF performance relationships of the Pd<sub>0.1</sub>/CN<sub>x</sub> catalysts

The RCF activities of the Pd<sub>0.1</sub>/CN<sub>x</sub> catalysts synthesized using the WI, CI, and DP methods were different (Table 1). The LDPM yields decreased as follows: Pd<sub>0.1</sub>/CN<sub>x</sub>-DP4 (53.6 C%)  $\approx$  Pd<sub>0.1</sub>/CN<sub>x</sub>-CI8 (51.4 C%) > Pd<sub>0.1</sub>/CN<sub>x</sub>-WI (46.7 C%)  $\approx$  Pd<sub>0.1</sub>/CN<sub>x</sub>-CI4 (45.0 C%); on the other hand, the DODs decreased as follows: Pd<sub>0.1</sub>/CN<sub>x</sub>-DP4 (84.6 wt %)  $\approx$  Pd<sub>0.1</sub>/CN<sub>x</sub>-CI8 (84.0 wt %) > Pd<sub>0.1</sub>/CN<sub>x</sub>-CI4 (77.9 wt %)  $\approx$  Pd<sub>0.1</sub>/CN<sub>x</sub>-WI > (75.8 wt %). These results indicate that the Pd sites of the Pd<sub>0.1</sub>/CN<sub>x</sub> catalysts synthesized using the WI, CI, and DP methods exhibited different characteristics, which affected their ability to stabilize the decomposed lignin intermediates.

To examine the structure–performance relationships of the Pd<sub>0.1</sub>/CN<sub>x</sub> catalysts synthesized using the WI, CI, and DP methods, the physicochemical properties of the catalysts were determined. The Brunauer–Emmett–Teller (BET) surface area of the CN<sub>x</sub> support was high (1799.8 m<sup>2</sup> g<sup>−1</sup>); moreover, its N content was 1.9 wt%, which promoted tight anchoring of ultrasmall Pd nanoparticles (NPs) and single Pd atoms

on CN<sub>x</sub> by strong interaction between Pd and the defect and N-doped sites of CN<sub>x</sub> [43]. The measured Pd contents of the Pd<sub>0.1</sub>/CN<sub>x</sub> catalysts ranged between 0.108 and 0.126 wt% (Table S3). The textural properties of the Pd<sub>0.1</sub>/CN<sub>x</sub> catalysts were similar to those of the CN<sub>x</sub> support (data not reported), indicating that the low Pd loading and metal loading method did not affect the specific surface area and porosity of the catalysts. The size of the Pd NPs of the Pd<sub>0.1</sub>/CN<sub>x</sub> catalysts depended on the metal loading method, as illustrated in the low-magnification HAADF–STEM images of the Pd<sub>0.1</sub>/CN<sub>x</sub>-WI, Pd<sub>0.1</sub>/CN<sub>x</sub>-CI4, Pd<sub>0.1</sub>/CN<sub>x</sub>-CI8, and Pd<sub>0.1</sub>/CN<sub>x</sub>-DP4 catalysts (Fig. 2a, c, e, and g, respectively). The average Pd NP size decreased as follows: Pd<sub>0.1</sub>/CN<sub>x</sub>-WI (5.98 nm) > Pd<sub>0.1</sub>/CN<sub>x</sub>-CI4 (4.49 nm) > Pd<sub>0.1</sub>/CN<sub>x</sub>-CI8 (3.35 nm)  $\approx$  Pd<sub>0.1</sub>/CN<sub>x</sub>-DP4 (3.44 nm); furthermore, the total number of Pd NPs decreased as follows: Pd<sub>0.1</sub>/CN<sub>x</sub>-CI4 (58) > Pd<sub>0.1</sub>/CN<sub>x</sub>-WI (44) > Pd<sub>0.1</sub>/CN<sub>x</sub>-CI8 (11) = Pd<sub>0.1</sub>/CN<sub>x</sub>-DP4 (11). Therefore, the growth of the Pd NPs of the Pd<sub>0.1</sub>/CN<sub>x</sub>-CI8 and Pd<sub>0.1</sub>/CN<sub>x</sub>-DP4 catalysts was more effectively suppressed than that of the Pd NPs of the Pd<sub>0.1</sub>/CN<sub>x</sub>-WI and Pd<sub>0.1</sub>/CN<sub>x</sub>-CI4 catalysts. The presence of Pd single atoms and

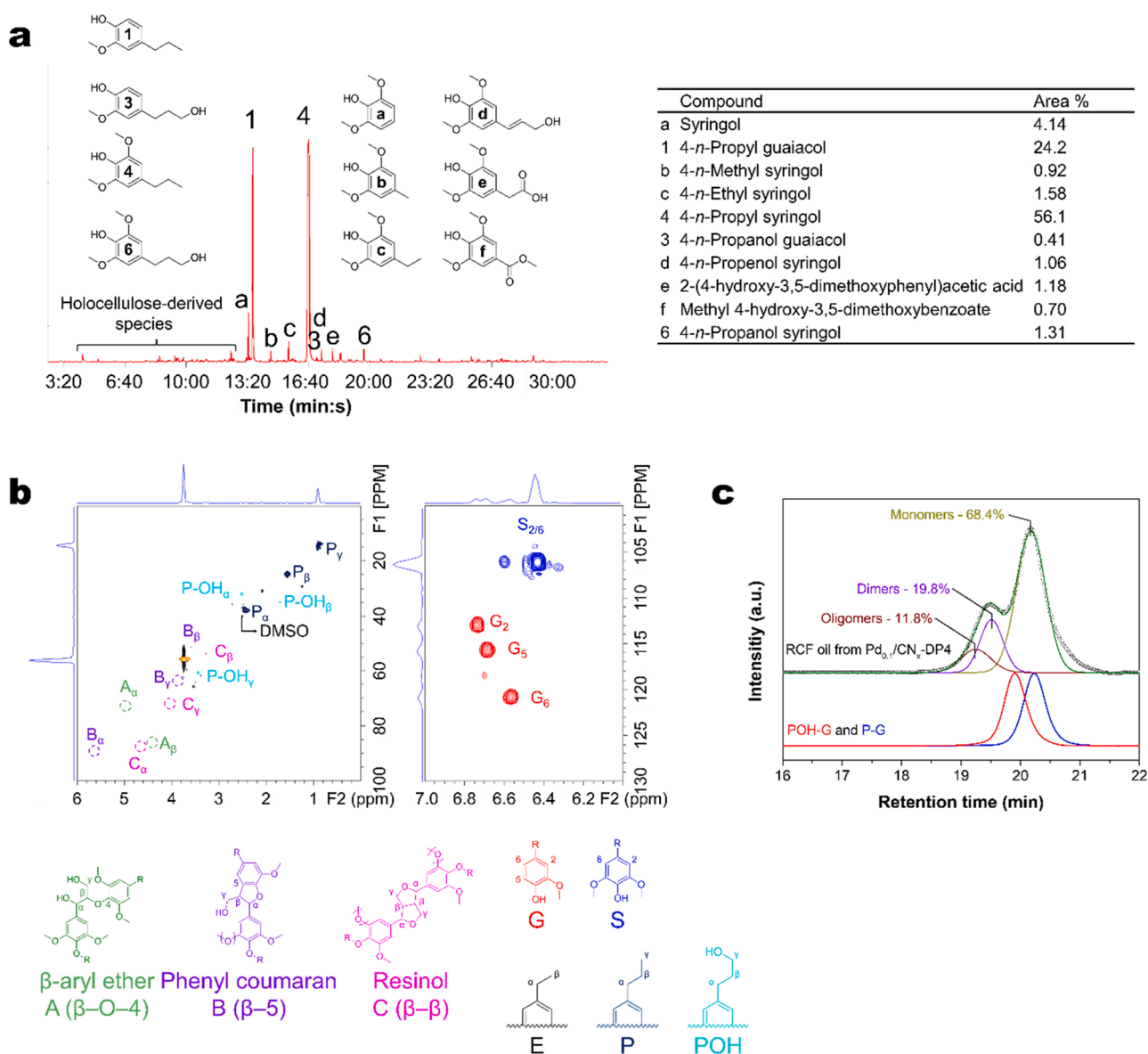


**Fig. 3.** (a) Gas chromatography–time-of-flight/mass spectroscopy profiles, (b) two-dimensional heteronuclear single quantum coherence nuclear magnetic resonance spectra and (c) gel permeation chromatography of the dichloromethane-soluble organics produced over Pd<sub>0.1</sub>/CN<sub>x</sub>-DP4. Reaction conditions: 3 g of birch wood, 0.45 g of catalyst, 60 mL of methanol, initial H<sub>2</sub> pressure of 3.0 MPa, 250 °C, 3 h. Pd<sub>0.1</sub>/CN<sub>x</sub>-DP4 designates 0.1 wt% Pd on N-doped carbon synthesized via deposition–precipitation with urea (urea/Pd molar ratio = 4) and DMSO denotes dimethyl sulfoxide.



nanoclusters was observed in the high magnified HAADF-STEM images of the Pd<sub>0.1</sub>/CN<sub>x</sub>-WI, Pd<sub>0.1</sub>/CN<sub>x</sub>-CI4, Pd<sub>0.1</sub>/CN<sub>x</sub>-CI8, and Pd<sub>0.1</sub>/CN<sub>x</sub>-DP4 catalysts (Fig. 2b, d, f, and h, respectively).

The electronic states and local chemical bonding structures of Pd in the Pd<sub>0.1</sub>/CN<sub>x</sub> catalysts were investigated using XAS. In the XANES profiles, the intensity of the white line of the Pd<sub>0.1</sub>/CN<sub>x</sub>-DP4 catalyst was higher than those of the other Pd<sub>0.1</sub>/CN<sub>x</sub> catalysts (Fig. 2i). In addition, the first derivative profiles of the Pd K-edge XANES spectra revealed that the intensities of the near-edge peaks at approximately 24384 eV decreased as follows: Pd foil > Pd<sub>0.1</sub>/CN<sub>x</sub>-WI ≈ Pd<sub>0.1</sub>/CN<sub>x</sub>-CI4 ≈ Pd<sub>0.1</sub>/CN<sub>x</sub>-CI8 > Pd<sub>0.1</sub>/CN<sub>x</sub>-DP4 > PdO (Fig. 2j). Accordingly, the positive charge of the Pd species in the Pd<sub>0.1</sub>/CN<sub>x</sub>-DP4 was the highest among all the Pd<sub>0.1</sub>/CN<sub>x</sub> catalysts. The presence of higher-valent Pd species in the Pd<sub>0.1</sub>/CN<sub>x</sub>-DP4 indicated the preferential formation of Pd<sup>δ+</sup>-N/C/O bonds over Pd-Pd bonds [44], resulting in the larger number of single Pd atoms. The intensities of the Pd-Pd peaks at 2.51 Å in the Pd K-edge EXAFS spectra of Pd, PdO, and the Pd-based catalysts decreased as follows: Pd foil > Pd<sub>0.1</sub>/CN<sub>x</sub>-CI4 > Pd<sub>0.1</sub>/CN<sub>x</sub>-WI > Pd<sub>0.1</sub>/CN<sub>x</sub>-CI8 > Pd<sub>0.1</sub>/CN<sub>x</sub>-DP4 > PdO (Fig. 3k). To estimate the coordination numbers (CNs) of Pd and bond lengths (R) by fitting the EXAFS profiles, a model single Pd atom surrounded by four identical pyridine structures was constructed (Fig. S12). The CNs of Pd-Pd decreased as follows: Pd<sub>0.1</sub>/CN<sub>x</sub>-CI4 (3.57) > Pd<sub>0.1</sub>/CN<sub>x</sub>-WI (3.31) > Pd<sub>0.1</sub>/CN<sub>x</sub>-CI8 (2.98) > Pd<sub>0.1</sub>/CN<sub>x</sub>-DP4 (2.93) (Table S4). Therefore, the Pd sites of Pd<sub>0.1</sub>/CN<sub>x</sub>-DP4 were more dispersed than those of the other Pd<sub>0.1</sub>/CN<sub>x</sub> catalysts. The CNs of Pd-N (2.41) and Pd-C (2.46) of Pd<sub>0.1</sub>/CN<sub>x</sub>-WI were similar, and the lengths of the Pd-N and Pd-C bonds (2.01 and 2.76 Å, respectively) were similar to those of the model Pd-pyridine structure (Pd-N, 1.98 Å; Pd-C, 2.83 Å; Fig. S12a). Hence, it was reasonable to hypothesize that the single Pd atoms of the Pd<sub>0.1</sub>/CN<sub>x</sub>-WI were anchored to CN<sub>x</sub> via Pd-N-C bonds, and the formation of Pd-C bonds was suppressed. The Pd<sub>0.1</sub>/CN<sub>x</sub>-CI4 catalyst comprised numerous Pd NPs (Fig. 2c); therefore, the CNs of Pd-Pd (3.57), Pd-N (1.53) and Pd-C (1.05) were higher, lower, and lower, respectively, than that of Pd<sub>0.1</sub>/CN<sub>x</sub>-WI (Pd-Pd, 3.31; Pd-N, 2.41, Pd-C, 2.46). The ratio of the CNs of Pd-N and Pd-C of Pd<sub>0.1</sub>/CN<sub>x</sub>-CI8 (0.6) was lower than that of the Pd<sub>0.1</sub>/CN<sub>x</sub>-WI (1.0) and Pd<sub>0.1</sub>/CN<sub>x</sub>-CI4 (1.5) catalysts. In addition, the Pd-C bonds of the Pd<sub>0.1</sub>/CN<sub>x</sub>-CI8 (2.67 Å) were shorter than the Pd-pyridine bonds (2.96 Å). Consequently, Pd-N-C and Pd-C interactions coexisted in the Pd<sub>0.1</sub>/CN<sub>x</sub>-CI8 catalyst. The ratio of the CNs of Pd-N and Pd-C of Pd<sub>0.1</sub>/CN<sub>x</sub>-DP4 (0.3) was significantly lower than those of the other Pd<sub>0.1</sub>/CN<sub>x</sub> catalysts (0.6–1.5). In addition, the Pd-C bonds (2.47 Å) of Pd<sub>0.1</sub>/CN<sub>x</sub>-DP4 were shorter than those of the other Pd<sub>0.1</sub>/CN<sub>x</sub> catalysts (2.67–2.86 Å). Therefore, the single Pd atoms of the Pd<sub>0.1</sub>/CN<sub>x</sub>-DP4 and Pd<sub>0.1</sub>/CN<sub>x</sub>-CI8 catalysts were located at both the N-doped and C<sub>3</sub>N<sub>1</sub> sites, whereas those of Pd<sub>0.1</sub>/CN<sub>x</sub>-CI4 and Pd<sub>0.1</sub>/CN<sub>x</sub>-WI were primarily located at the N-doped sites. The microstructures of the Pd<sub>0.1</sub>/CN<sub>x</sub> catalysts synthesized using the WI, CI, and DP methods are presented in Fig. S13 and discussed in Supplementary data E. The relationship between catalyst structure (Fig. 2) and RCF performance (Table 1) revealed that highly dispersed single Pd atoms and Pd nanoclusters were more active than their poorly dispersed counterparts for stabilizing decomposed lignin intermediates; therefore, the re-adsorption of the decomposed lignin fractions on the solid pulp surface was suppressed. Accordingly, the superior RCF performance of the Pd<sub>0.1</sub>/CN<sub>x</sub>-DP4 and Pd<sub>0.1</sub>/CN<sub>x</sub>-CI8 catalysts was attributed to the suppression of Pd nanocluster growth.

The chemical composition of the DSOs obtained using the Pd<sub>0.1</sub>/CN<sub>x</sub>-DP4 catalyst, which was analyzed using GC-TOF/MS, is presented in Fig. 3a and Table S2. The LDPs primarily consisted of 4-*n*-propyl guaiacol (P-G) and 4-*n*-propyl syringol (P-S) (peaks 1 and 4, respectively, Fig. 3a) and several minor compounds, viz. 4-*n*-propanol guaiacol (POH-G), 4-*n*-propanol syringol (POH-S), syringol, 4-*n*-methyl syringol, 4-*n*-ethyl syringol, 4-*n*-propenol syringol, 2-(4-hydroxy-3,5-dimethoxyphenyl)acetic acid, and methyl 4-hydroxy-3,5-dimethoxybenzoate (Fig. 3a, peaks 3, 6, a, b, c, d, e, and f, respectively). The propyl-to-

propanol ratio (P/POH) in the LDPs produced over the Pd<sub>0.1</sub>/CN<sub>x</sub>-DP4 catalyst, was 15.9, which was significantly higher than those of the LDPs obtained over the Pd<sub>5</sub>/AC-0.015 (0.08) and the other Pd<sub>0.1</sub>/CN<sub>x</sub> catalysts (4.16–7.61). Therefore, the hydrodeoxygenation of the terminal C-OH bonds was more activated over the ultrasmall Pd sites of the Pd<sub>0.1</sub>/CN<sub>x</sub>-DP4 catalyst than over the Pd sites of the Pd<sub>5</sub>/AC-0.015 catalyst. The high selectivity of the Pd<sub>0.1</sub>/CN<sub>x</sub>-DP4 catalyst toward propyl-substituted guaiacol and syringol was beneficial for the subsequent synthesis of drop-in biofuel because the burden of metal catalyst to proceed hydrodeoxygenation can be reduced during the subsequent upgrading. Only a few holocellulose-derived species with very low area percentages (0.24–0.91%), such as glycolaldehyde dimethyl acetal, succinic acid, dimethyl ester, and 4,4-dimethoxy-butanoic acid methyl ester, were present in the DSOs. The primary peaks in the 2D HSQC NMR spectra of the DSOs obtained using the Pd<sub>0.1</sub>/CN<sub>x</sub>-DP4 catalyst were associated with 4-*n*-propyl (alkyl branch peaks in the ranges of 0–3 ppm (H<sup>1</sup>) and 10–40 ppm (C<sup>13</sup>)) guaiacol (G<sub>2</sub>, G<sub>5</sub>, and G<sub>6</sub> peaks in the ranges of 6.6–6.8 ppm (H<sup>1</sup>) and 110–125 ppm (C<sup>13</sup>)), and syringol (S<sub>2/6</sub> peaks in the ranges of 6.2–6.6 ppm (H<sup>1</sup>) and 105–110 ppm (C<sup>13</sup>)). No peaks associated with β-aryl ether (β-O-4) were observed, and very weak peaks ascribed to phenyl coumaran (β-5) and resinol (β-β) were detected in the 2D HSQC NMR spectra. The high LDPM content, and absence of the β-O-4 peak and weak β-5 and β-β peaks in the 2D HSQC NMR spectra of the DSOs indicate that effective depolymerization and stabilization of LDPs occurred using the Pd<sub>0.1</sub>/CN<sub>x</sub>-DP4 catalyst. The molecular weight distribution of DSOs was analyzed using GPC (Fig. 3c). The GPC profile was deconvoluted into three peaks; the peaks at 20.17, 19.51 and 19.25 min indicated the presence of monomers, dimers and oligomers, respectively. The area% of monomers, dimers and oligomers peaks were 68.4%, 19.8% and 11.8%, respectively.

#### 3.4. PRS conversion over Ni<sub>2</sub>@Al<sub>2</sub>O<sub>3</sub>/AC

To evaluate the usability of the PRS collected after RCF, enzymatic hydrolysis to produce glucose [45,46], catalytic reaction in a biphasic solvent system to produce gasoline-fraction fuels [18], and catalytic reaction in methanol to produce C<sub>4</sub>–C<sub>6</sub> alcohols [19] have been studied previously. The conversion of PRS over the Pd<sub>0.1</sub>/CN<sub>x</sub>-DP4 catalyst embedded into its matrix produced ketonic species (Fig. S14). The primary products included cyclopentanone (CPO, 1.63 C%), 2-methyl CPO (4.11 C%), 3-methyl CPO (0.42 C%), 2-methyl-2-cyclopentene-1-one (3.24 C%), 3-methyl-2-cyclopentene-1-one (0.72 C%), and 2,5-hexanedione (3.29 C%). However, the total yield of ketonic species was low (19.6 C%); moreover, no diols and monocarboxylic acids were produced (entry 1, Table 2). Herein, we used a new approach for converting the PRS into high-yield diols and monocarboxylic acids over passivated Ni<sub>2</sub>@Al<sub>2</sub>O<sub>3</sub>/AC.

The properties of the Ni<sub>2</sub>@Al<sub>2</sub>O<sub>3</sub>/AC catalyst are illustrated in Fig. 4. The average size of the Ni NPs and BET surface area of the Ni<sub>2</sub>@Al<sub>2</sub>O<sub>3</sub>/AC catalyst were 15.3 nm and 312 m<sup>2</sup> g<sup>-1</sup>, respectively. The core-shell structure of Ni<sub>2</sub>@Al<sub>2</sub>O<sub>3</sub>/AC was proved by the STEM-EDS images (Fig. S15). The peaks at 44.5°, 51.8°, and 76.4° in the XRD pattern of the passivated Ni<sub>2</sub>@Al<sub>2</sub>O<sub>3</sub>/AC catalyst were ascribed to the (111), (200), and (220) planes, respectively, of metallic Ni, whereas the peaks at 37.2°, 43.3°, 62.9°, 75.4°, and 79.4° were attributed to the (111), (200), (220), (311), and (222) planes, respectively, of NiO. The crystalline sizes of the Ni (111) plane of the non-passivated and passivated Ni<sub>2</sub>@Al<sub>2</sub>O<sub>3</sub>/AC were calculated to be 11.8 and 6.8 nm, respectively, using the Scherrer equation. The Ni 2p<sub>1/2</sub> and Ni 2p<sub>3/2</sub> XPS profiles of the passivated Ni<sub>2</sub>@Al<sub>2</sub>O<sub>3</sub>/AC catalyst were deconvoluted into four peaks. The peaks at 853.5 and 870.8 eV, which were associated with the Ni<sup>2+</sup> 2p<sub>3/2</sub> and 2p<sub>1/2</sub> species, respectively, and the Ni<sup>2+</sup> satellite peaks at 860.5 and 877.8 eV [47,48]. These results indicate that the surface of the Ni NPs was almost completely oxidized to NiO. The NH<sub>3</sub>-TPD profile of the passivated Ni<sub>2</sub>@Al<sub>2</sub>O<sub>3</sub>/AC catalyst and its corresponding QMS profiles are illustrated in Fig. 4g–i. According to the QMS profiles, the



**Table 2**

Conversion, carbon yields of the holocellulose-derived products, and gas yields for the conversion of pulp-rich solid (PRS) obtained via reductive catalytic fractionation (RCF) over the Pd<sub>0.1</sub>/CN<sub>x</sub>-DP4 and passivated Ni<sub>2</sub> @Al<sub>2</sub>O<sub>3</sub>/AC + Pd<sub>0.1</sub>/CN<sub>x</sub>-DP4 catalysts and for the conversion of carbohydrates over the passivated Ni<sub>2</sub> @Al<sub>2</sub>O<sub>3</sub>/AC catalyst.<sup>a</sup> Pd<sub>0.1</sub>/CN<sub>x</sub>-DP4, and Ni<sub>2</sub> @Al<sub>2</sub>O<sub>3</sub>/AC denote 0.1 wt% Pd on N-doped carbon synthesized via deposition–precipitation using urea (urea/Pd molar ratio = 4), and Ni–alumina core–shell catalyst on activated carbon (Ni/Al molar ratio = 2), respectively.

Entry	Feedstock	Catalyst	Conversion (wt%) <sup>b</sup>	Carbon yields of the holocellulose-derived products (C%) <sup>c</sup>													Gas yield (C%) <sup>d</sup>
				EG	1,2- PG	1,2- BD	1,2- PD	1,2- HD	GR	AA	PA	BA	VA	HA	LA	Total	
1 <sup>e</sup>	PRS from RCF	Pd <sub>0.1</sub> /CN <sub>x</sub> -DP4	91.2	N. D. <sup>f</sup>	N.D.	N.D.	N.D.	N.D.	N. D.	N. D.	N. D.	N. D.	N. D.	N. D.	N. D.	19.6 <sup>g</sup>	N.D.
2 <sup>h</sup>	PRS from RCF	Passivated Ni <sub>2</sub> @Al <sub>2</sub> O <sub>3</sub> /AC <sup>i</sup> + Pd <sub>0.1</sub> /CN <sub>x</sub> - DP4	91.5	9.48	11.7	6.07	2.86	0.20	6.04	1.78	2.33	8.31	N. D.	0.60	1.67	51.1	5.79
3 <sup>i</sup>	Cellulose	Passivated Ni <sub>2</sub> @Al <sub>2</sub> O <sub>3</sub> /AC <sup>i</sup>	98.9	6.42	8.71	5.43	3.27	1.96	5.53	1.30	5.10	1.08	1.66	1.85	3.76	46.1	11.1
4 <sup>j</sup>	Glucose	Passivated Ni <sub>2</sub> @Al <sub>2</sub> O <sub>3</sub> /AC <sup>i</sup>	99.6	3.95	19.1	3.61	1.18	3.22	1.76	3.24	3.99	5.91	1.17	3.89	3.51	54.5	2.88
5 <sup>j</sup>	Fructose	Passivated Ni <sub>2</sub> @Al <sub>2</sub> O <sub>3</sub> /AC <sup>i</sup>	99.7	3.47	22.7	2.67	1.48	2.91	2.75	3.09	0.98	8.19	3.19	3.42	4.79	59.6	4.26

<sup>a</sup> EG, 1,2-PG, 1,2-BD, 1,2-PD, 1,2-HD, GR, AA, PA, BA, VA, HA, and LA denote ethylene glycol, 1,2-propanediol, 1,2-butanediol, 1,2-pentanediol, 1,2-hexanediol, glycerol, acetic acid, propionic acid, butyric acid, valeric acid, hexanoic acid, and lactic acid, respectively.

<sup>b</sup> Based on the weight of the dried ash-free feedstock.

<sup>c</sup> Based on the carbon content of carbohydrates in the feedstock. The detailed description of the carbon yields calculation of the holocellulose-derived products is included in [Supplementary data D](#).

<sup>d</sup> Based on the C content of carbohydrates in the feedstock. The primary gas species, which were analyzed using a refinery gas analyzer–gas chromatography instrument, were CO<sub>2</sub> and CO ([Fig. S22](#)).

<sup>e</sup> Reaction conditions: 1.81 g of PRS mixed with 0.45 g of Pd<sub>0.1</sub>/CN<sub>x</sub>, 40 mL of water, initial H<sub>2</sub> pressure of 3.0 MPa, 270 °C, 1 h.

<sup>f</sup> N.D., Not detected

<sup>g</sup> Polyols and carboxylic acids were not detected. The products included cyclopentanone and its derivatives ([Fig. S14](#)).

<sup>h</sup> Reaction conditions: 1.81 h of PRS mixed with 0.45 g of Pd<sub>0.1</sub>/CN<sub>x</sub>, 1 g of passivated Ni<sub>2</sub> @Al<sub>2</sub>O<sub>3</sub>/AC, 40 mL of water, initial H<sub>2</sub> pressure of 3.0 MPa, 270 °C, 1 h.

<sup>i</sup> Passivation conditions: 200 °C, 4 h, 21% O<sub>2</sub>/N<sub>2</sub> flow of 100 mL min<sup>−1</sup>.

<sup>j</sup> Reaction conditions: 2 g of carbohydrate, 1 g of catalyst, 40 mL of water, initial H<sub>2</sub> pressure of 3.0 MPa, 270 °C, 1 h.

peaks at 225 and 553 °C in the NH<sub>3</sub>–TPD profile of the passivated Ni<sub>2</sub> @Al<sub>2</sub>O<sub>3</sub>/AC catalyst were ascribed to the desorption of NH<sub>3</sub> and desorption of CO<sub>2</sub> generated via the decarboxylation of the residual oxygenated functionalities of AC, respectively ([Supplementary data F](#)). The total acidity of the passivated Ni<sub>2</sub> @Al<sub>2</sub>O<sub>3</sub>/AC catalyst was 0.184 mmol g<sup>−1</sup>. The peak at 192 °C in the NH<sub>3</sub>–TPD profile of Pd<sub>0.1</sub>/CN<sub>x</sub>-DP4 corresponded to its weak acid sites, and the total acidity of the Pd<sub>0.1</sub>/CN<sub>x</sub>-DP4 catalyst was 0.081 mmol g<sup>−1</sup> ([Fig. S16, Supplementary data F](#)). Therefore, the conversion of PRS occurred over the metallic and acid sites of the passivated Ni<sub>2</sub> @Al<sub>2</sub>O<sub>3</sub>/AC and Pd<sub>0.1</sub>/CN<sub>x</sub>-DP4 catalysts.

The conversion and polyol and monocarboxylic acid yields for the reaction of the PRS embedded with Pd<sub>0.1</sub>/CN<sub>x</sub>-DP4 over the passivated Ni<sub>2</sub> @Al<sub>2</sub>O<sub>3</sub>/AC catalyst were 91.5 wt%, 36.4 C%, and 14.7 C%, respectively (entry 2, [Table 2](#)). The polyols included EG, 1,2-PG, 1,2-BG, 1,2-PD, 1,2-HD, and GR, while the monocarboxylic acids included AA, PA, BA, VA, HA, and LA. A typical GC–TOF/MS profile of the liquid products of the PRS conversion is presented in [Fig. S17](#). A fraction of the residual lignin in the PRS was converted into P–G and P–S. The liquids collected after the reaction over the absence and presence of passivated Ni<sub>2</sub> @Al<sub>2</sub>O<sub>3</sub>/AC catalyst were yellowish and clear, respectively ([Fig. S18](#)). This indicated that humin formation was suppressed in the presence of the passivated Ni<sub>2</sub> @Al<sub>2</sub>O<sub>3</sub>/AC catalyst. The formation of high-molecular-weight species in the absence of the passivated Ni<sub>2</sub> @Al<sub>2</sub>O<sub>3</sub>/AC catalyst was demonstrated using GFC data ([Fig. S19, Table S6](#)). When the passivated Ni<sub>2</sub> @Al<sub>2</sub>O<sub>3</sub>/AC and Pd<sub>0.1</sub>/CN<sub>x</sub>-DP4 catalysts were used, the percentage of chemical species with lower molecular weights than that of glucose (180 g mol<sup>−1</sup>) in the liquid product exceeded 94%, whereas the corresponding percentage for the reaction over the Pd<sub>0.1</sub>/CN<sub>x</sub>-DP4 catalyst was only 76%. The conversion (98.9 wt%), polyol yield (31.3 C%) and monocarboxylic acid yield (14.8%) for the conversion of cellulose over the passivated Ni<sub>2</sub> @Al<sub>2</sub>O<sub>3</sub>/AC catalyst (entry 3, [Table 2](#)) were slightly higher, slightly lower, and similar to those for the PRS conversion over the Pd<sub>0.1</sub>/CN<sub>x</sub>-DP4 and

passivated Ni<sub>2</sub> @Al<sub>2</sub>O<sub>3</sub>/AC catalysts. The similar conversions and product selectivities of the PRS and microcrystalline cellulose indicate that the residual lignin fractions and Pd<sub>0.1</sub>/CN<sub>x</sub>-DP4 catalyst in the RCF pulp (approximately 30 wt% = Pd<sub>0.1</sub>/CN<sub>x</sub>-DP4 (20 wt%) + lignin (5 wt%) + others (5 wt%); [Fig. S20a](#)) did not inhibit the conversion of holocellulose. The residual lignin fraction in the PRS contributed to the solid residue; consequently, the conversion of PRS was lower than that of cellulose. Because of the heterogeneous nature of the feedstocks and numerous consecutive reaction pathways to obtain the targeted products, it was difficult to determine why the polyol and monocarboxylic acid yields obtained from the RCF pulp were higher than those obtained from microcrystalline cellulose. A plausible reason was the low crystallinity of the RCF pulp. The crystallinity index of the RCF pulp (69.4%), which was calculated using the XRD peak height method [49], was significantly lower than that of microcrystalline cellulose (81.0%, [Fig. S21](#)). In addition, the lower yields of polyols and monocarboxylic acids obtained from cellulose were ascribed to the yield of gases produced from cellulose being higher than that of gases produced from the RCF pulp ([Fig. S22](#)).

To examine the role of catalyst passivation during the PRS conversion, the conversion of cellulose over the Ni<sub>2</sub> @Al<sub>2</sub>O<sub>3</sub>/AC catalysts passivated under various conditions was explored ([Fig. S23](#)). The polyol and monocarboxylic acid yield (21.4 C%) and gas yield (37.4 C%) over the non-passivated Ni<sub>2</sub> @Al<sub>2</sub>O<sub>3</sub>/AC catalyst were lower and higher, respectively, than those over the passivated Ni<sub>2</sub> @Al<sub>2</sub>O<sub>3</sub>/AC catalyst. The metallic Ni sites are active for cellulose gasification under sub- and supercritical water conditions [50]. As the passivation time and O<sub>2</sub> content of the passivation sweep fluid were increased, gasification was suppressed and the selectivity toward polyols and monocarboxylic acids increased.

To investigate the plausible reaction pathways of the PRS over the passivated Ni<sub>2</sub> @Al<sub>2</sub>O<sub>3</sub>/AC catalysts, the conversion of monosaccharides was evaluated. The polyol and monocarboxylic acid yields achieved when glucose was used as the feedstock were 32.8 and 21.7 C%,

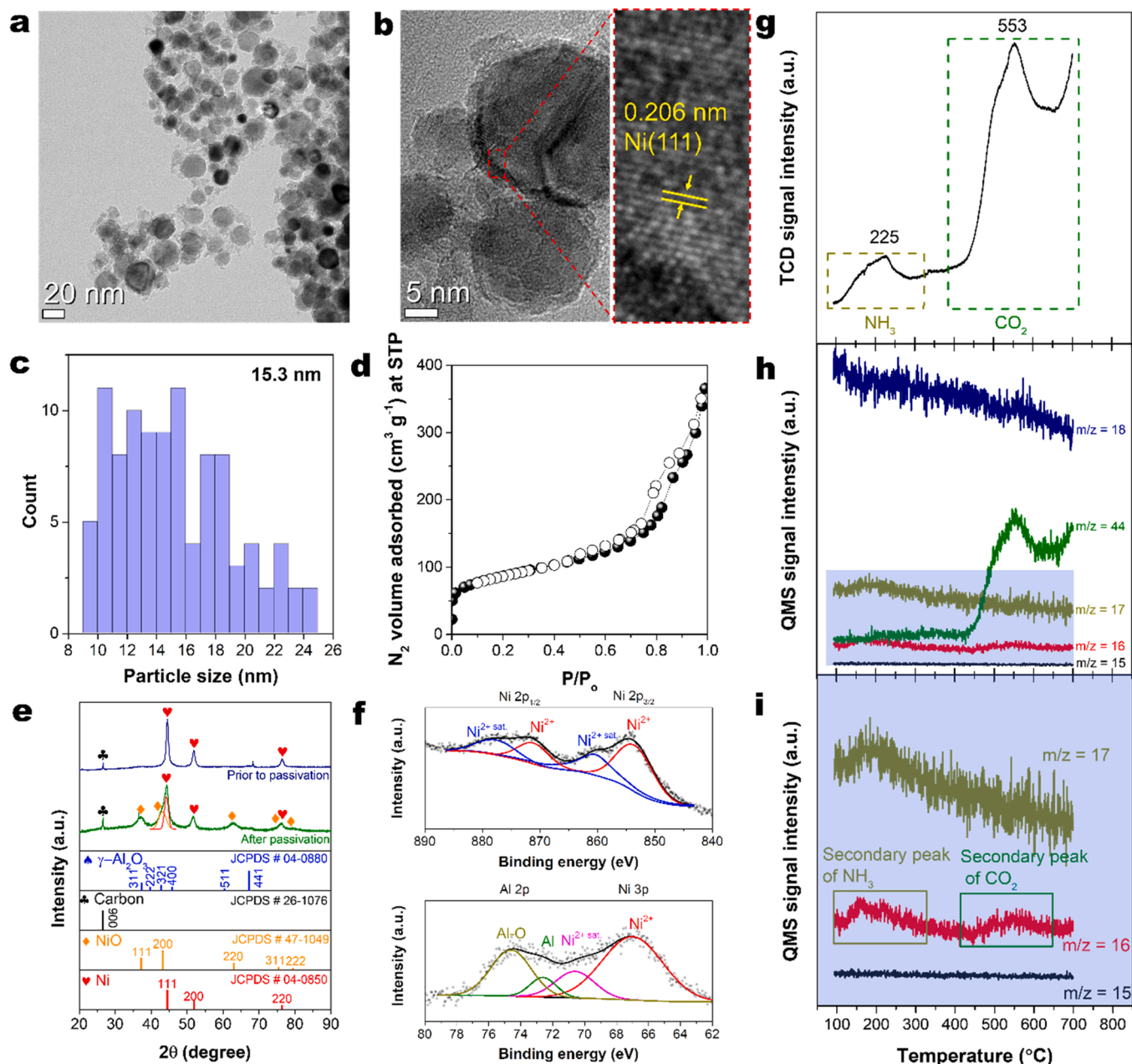


**Fig. 4.** (a) and (b) High-resolution transmission electron microscopy images, (c) Ni particle size distribution, (d)  $N_2$  adsorption–desorption isotherm, (e) X-ray diffraction patterns, (f) high-resolution Ni 2p, Ni 3p, and Al 2p X-ray photoelectron spectroscopy profiles, and (g)  $NH_3$ –temperature-programmed desorption (TPD) profile of the passivated  $Ni_2 @Al_2O_3/AC$  catalyst. (h) and (i) Quadrupole mass spectroscopy (QMS) profiles of the gas species emitted from the TPD cell during  $NH_3$  desorption.  $Ni_2 @Al_2O_3/AC$  denotes Ni–alumina core–shell catalyst on activated carbon (Ni/Al molar ratio = 2).

respectively. Similar polyol and monocarboxylic acid yields (36.0 and 23.7 C%, respectively) were achieved when fructose was used as the feedstock. The  $C_3/(C_2 + C_4)$  compound ratios  $((PA + 1,2-PG + GR)/(AA + EG + BA + 1,2-BD))$  associated with the conversion of glucose and fructose were 1.48 and 1.52, respectively. Glucose was cleaved into  $C_2 + C_4$  keto-alcohols, and then, the  $C_4$  keto-alcohol was cleaved into a  $C_2$  keto-alcohol via retro-aldol condensation. Conversely, fructose was cleaved into  $C_3$  keto-alcohols via retro-aldol condensation over the Lewis acid sites (LASs) of the catalysts [51]. Therefore, the  $C_3$  compounds obtained from glucose and  $C_2$  and  $C_4$  compounds obtained from fructose indicate that the LASs of the passivated  $Ni_2 @Al_2O_3/AC$  catalysts promoted glucose and fructose isomerization. The conversion of cellulose into hydrolyzed (e.g., glucose), isomerized (e.g., fructose), dehydrated (e.g., 5-hydroxymethyl furfural and furfural), decomposed (e.

g., erythrose, glycolaldehyde, glyceraldehyde, and dihydroxyacetone), and hydrated products (e.g., LA and levulinic acid) under subcritical water conditions in the absence of catalysts has been discussed previously [52]. The high reactivity for cellulose hydrolysis, high solubility of the decomposed products, and high diffusivity of subcritical water (e.g., the relative permittivity,  $pK_w$  value, and self-diffusion coefficient of subcritical water at 270 °C and 8.0 MPa are 27.89 [53], 10.67 [54], and  $3 \times 10^{-4} \text{ cm}^2 \text{ s}^{-1}$  [55], respectively) render it an efficient medium for cellulose conversion. Under subcritical water conditions, the hydrolysis of cellulose to glucose and subsequent retro-aldol condensation of glucose to erythrose and glycolaldehyde can occur easily. In addition, glucose can isomerize into fructose, and dihydroxyacetone and glyceraldehyde can be produced by subsequent retro-aldol condensation of fructose. The hydrogenation of the decomposed species over the Ni sites

of Ni-based catalysts can produce polyols, such as EG, 1,2-PG, GR, and 1,2-BG (Fig. S24) [56,57]. Moreover, glucose hydrogenation to sorbitol can occur at the Ni sites of Ni-based catalysts in the presence of molecular  $H_2$  [58,59]. Subsequently, sorbitol can be converted into 1,2-HD via 1,2,6-hexanetriol at the Ni sites of Ni-based catalysts [60,61]. The dehydration and subsequent tautomerization of glyceraldehyde in subcritical water can produce pyruvaldehyde, and the hydration of pyruvaldehyde can produce LA. Thereafter, AA and PA can be produced via the hydrogenation of LA [62,63], and VA can be obtained via the ring-opening reaction of the  $\gamma$ -valerolactone produced from levulinic acid [64,65]. Moreover, the ring-opening reactions of  $\delta$ -valerolactone or  $\delta$ -hydroxy- $\gamma$ -valerolactone can produce VA. HA can be produced via the ring-opening reaction of the 5-methyl- $\delta$ -valerolactone synthesized via

the ring-closing reaction and subsequent hydrodeoxygenation of gluconic acid. Similarly, BA can be synthesized via the ring-opening reaction of the  $\gamma$ -butyrolactone produced through the ring-closing reaction and subsequent hydrodeoxygenation of erythronic acid. Gluconic and erythronic acids can be synthesized via aldehyde–water shift reactions using glucose and erythrose, respectively [66].

### 3.5. Reusability of the two-step cascade reaction catalysts

The previous sections described the fractionation of birch wood into LDPM-rich lignin oil and highly delignified PRS using the  $Pd_{0.1}/CN_x$ -DP4 and the conversion of the collected PRS into highly selective polyols and monocarboxylic acids over passivated  $Ni_2 @Al_2O_3/AC$ . The solid

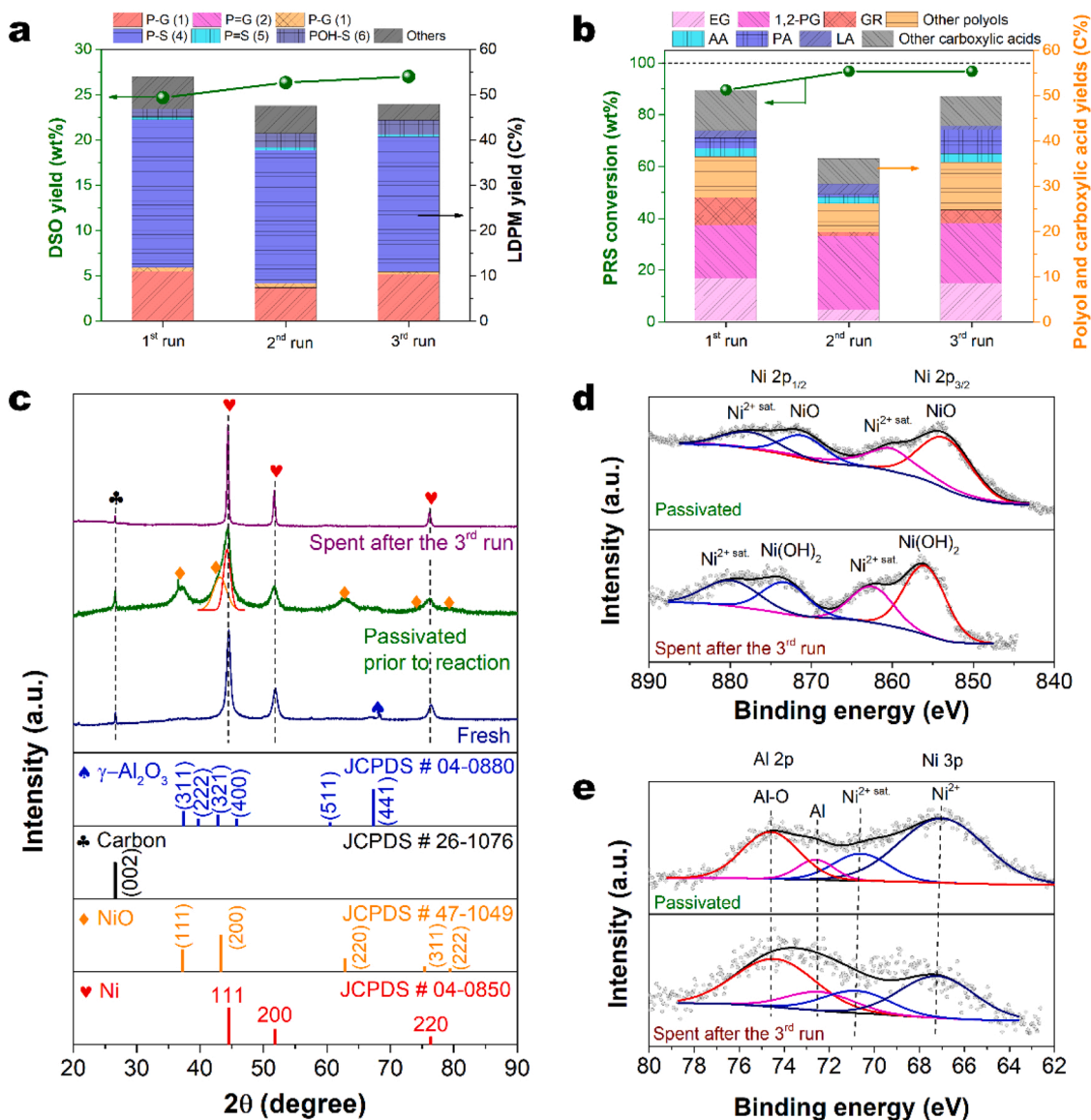


**Fig. 5.** Reusability test of magnetically separated  $Pd_{0.1}/CN_x$ -DP4 and  $Ni_2 @Al_2O_3/AC$  catalysts. (a) Dichloromethane-soluble organic (DSO) and lignin-derived phenolic monomer (LDPM) yields. Reaction conditions: 3 g of birch wood, 0.61–0.747 g of non-magnetic solid fraction (Table S7), 60 mL of methanol, initial  $H_2$  pressure of 3 MPa, 250 °C, 3 h. (b) Pulp-rich solid (PRS) conversion and polyol and monocarboxylic acid yields. Reaction conditions: 1.81 g of PRS, 0.61–0.747 g of non-magnetic solid fraction embedded in PRS, 1.08–0.80 g of magnetic solid fraction (Table S7), 40 mL of water, initial  $H_2$  pressure of 3 MPa, 270 °C, 1 h. (c) X-ray diffraction patterns, (d) high-resolution Ni 2p X-ray photoelectron spectroscopy (XPS) profiles, and (e) high-resolution Al 2p and Ni 3p XPS profiles of the freshly reduced, passivated, and spent  $Ni_2 @Al_2O_3/AC$  catalysts.  $Pd_{0.1}/CN_x$ -DP4 and  $Ni_2 @Al_2O_3/AC$  denote 0.1 wt% Pd on N-doped carbon synthesized via deposition–precipitation with urea (urea/Pd molar ratio of 4) and Ni–alumina core–shell catalyst on activated carbon (Ni/Al molar ratio = 2), respectively. P–G, P–G, POH–G, P–S, P–S, and POH–S designate 4-*n*-propyl guaiacol, 4-*n*-propenyl guaiacol, 4-*n*-propanol guaiacol, 4-*n*-propyl syringol, 4-*n*-propenyl syringol, and 4-*n*-propanol syringol, respectively. EG, 1,2-PG, GR, AA, PA, and LA denote ethylene glycol, 1,2-propanediol, glycerol, acetic acid, propionic acid, and lactic acid, respectively.



residue generated via the two-step cascade conversion of whole birch wood comprised  $\text{Pd}_{0.1}/\text{CN}_x\text{-DP4}$ , passivated  $\text{Ni}_2 @\text{Al}_2\text{O}_3/\text{AC}$ , unreacted/partially decomposed wood species, and tar/coke. Owing to their different magnetic properties (Fig. S25), the  $\text{Pd}_{0.1}/\text{CN}_x\text{-DP4}$  and  $\text{Ni}_2 @\text{Al}_2\text{O}_3/\text{AC}$  catalysts in the solid residue can be separated using a magnet. After the solid residue was dispersed in ethanol via sonication followed by magnetic separation, the amounts of the recovered  $\text{Pd}_{0.1}/\text{CN}_x\text{-DP4}$  and  $\text{Ni}_2 @\text{Al}_2\text{O}_3/\text{AC}$  catalysts in the non-magnetic and magnetic solids represented 70 and 83 wt%, respectively, of the initial amounts of catalysts (Fig. S26, Table S7). The amounts of  $\text{Pd}_{0.1}/\text{CN}_x\text{-DP4}$  and  $\text{Ni}_2 @\text{Al}_2\text{O}_3/\text{AC}$  that were not recovered (30 and 17 wt%, respectively, of the initial amounts) cross-contaminated the magnetically and non-magnetically recovered solid fractions, respectively.

Even though solid–solid separation using a magnet could not completely recover the catalysts used for the two-step cascade conversion, the RCF and PRS conversion activities of the spent catalysts were similar to those of the fresh catalysts. During the second RCF run over the non-magnetic solid fraction, the DSO yield increased slightly from 24.7 to 26.3 wt% and the LDPM yield decreased slightly from 53.6 to 47.5 C% (Fig. 5a). The lower LDPM yield during the second RCF run was attributed to the decrease in catalyst-to-feed ratio from 0.15 (fresh) to 0.11 (spent). To examine this hypothesis, RCF was conducted over fresh  $\text{Pd}_{0.1}/\text{CN}_x\text{-DP4}$  at a catalyst-to-feed ratio of 0.11 (Fig. S27). The DSO and LDPM yields over the fresh and spent  $\text{Pd}_{0.1}/\text{CN}_x\text{-DP4}$  catalysts were similar, indicating the activity of the catalyst was maintained. The DSO and LDPM yields and distribution of the LDPMs obtained after the third RCF run over the spent catalyst collected from the second RCF run were similar (27.0 wt% and 47.9 C%, respectively) to those obtained after the second RCF run (26.3 wt% and 47.5 C%, respectively, Fig. 5a). Therefore, the change in RCF performance of the spent  $\text{Pd}_{0.1}/\text{CN}_x\text{-DP4}$  catalyst retrieved from the non-magnetically recovered solid was negligible, and the presence of the passivated  $\text{Ni}_2 @\text{Al}_2\text{O}_3/\text{AC}$  catalyst and residual organic species did not diminish the RCF activity of the spent  $\text{Pd}_{0.1}/\text{CN}_x\text{-DP4}$  catalyst.

The polyol and monocarboxylic acid yield of the second PRS conversion over the magnetically recovered solid (36.0 C%) was smaller than that of the first PRS conversion over the fresh  $\text{Ni}_2 @\text{Al}_2\text{O}_3/\text{AC}$  catalyst (51.1 C%) (Fig. 5b). The decrease in activity of the spent  $\text{Ni}_2 @\text{Al}_2\text{O}_3/\text{AC}$  catalyst was ascribed to several reasons, including the loss of a fraction of  $\text{Ni}_2 @\text{Al}_2\text{O}_3/\text{AC}$  during the magnetic solid–solid separation, deposition of coke on the active sites at the catalyst surface, and changes in the electronic state of the metal sites. Only 58 wt% of the fresh  $\text{Ni}_2 @\text{Al}_2\text{O}_3/\text{AC}$  catalyst was retrieved from the magnetically recoverable solid after the second run (Table S7), indicating that the loss of magnetic properties was caused by the changes in the oxidation state of the spent  $\text{Ni}_2 @\text{Al}_2\text{O}_3/\text{AC}$  catalyst during the reaction. To recover the activity of the spent  $\text{Ni}_2 @\text{Al}_2\text{O}_3/\text{AC}$  catalyst, the magnetic solid collected after the second run was reactivated as follows. The solid was heat-treated at 300 °C for 1 h under an air flow of 100 mL min<sup>−1</sup> to burn out the coke or other organic species deposited on the catalyst surface and avoid burning the  $\text{CN}_x$  and AC (which start to burn at approximately 400 °C (Fig. S26a) and 500 °C (Fig. S26b), respectively) in the catalyst. Thereafter, the coke-free catalyst was reduced at 800 °C for 6 h under a 5%  $\text{H}_2/\text{Ar}$  flow of 100 mL min<sup>−1</sup>, and lastly passivated at 200 °C for 4 h under a 21%  $\text{O}_2/\text{N}_2$  flow of 100 mL min<sup>−1</sup>. The activity of the reactivated  $\text{Ni}_2 @\text{Al}_2\text{O}_3/\text{AC}$  catalyst for producing polyols and monocarboxylic acids during the third run (49.8 C%) was comparable to that of the fresh  $\text{Ni}_2 @\text{Al}_2\text{O}_3/\text{AC}$  catalyst (51.1 C%, Fig. 5b). In summary, the  $\text{Pd}_{0.1}/\text{CN}_x\text{-DP4}$  and passivated  $\text{Ni}_2 @\text{Al}_2\text{O}_3/\text{AC}$  catalysts exhibited good recyclability up to third run. To avoid the cross contamination between the  $\text{Pd}_{0.1}/\text{CN}_x\text{-DP4}$  and  $\text{Ni}_2 @\text{Al}_2\text{O}_3/\text{AC}$  catalyst and to further understand the stability of the  $\text{Ni}_2 @\text{Al}_2\text{O}_3/\text{AC}$  catalyst, the reusability of the  $\text{Ni}_2 @\text{Al}_2\text{O}_3/\text{AC}$  catalyst in the microcrystalline cellulose conversion up to fifth run was performed, and the results is shown in Fig. S28. The cellulose conversion and the yields of polyols and monocarboxylic acids were maintained up to the third run. In the subsequent fourth and fifth

runs, the yields of polyols and monocarboxylic acids steadily decreased.

To further investigate the deactivation mechanisms of the catalysts, the spent  $\text{Pd}_{0.1}/\text{CN}_x\text{-DP4}$  and  $\text{Ni}_2 @\text{Al}_2\text{O}_3/\text{AC}$  catalysts collected after the third run were analyzed. The ICP–MS results indicated that the total Pd, Ni, and Al contents of the spent catalysts (0.445, 311, and 89.1 mg, respectively) were slightly lower than those of the fresh catalysts (0.486, 344, and 90.9, respectively). Considering that coke was deposited on the surfaces of the spent catalysts, the ICP–MS data were rough estimates; however, the results indicated that metal leaching during the two-step cascade reaction was negligible. The Ni 2p XPS profile of the spent  $\text{Ni}_2 @\text{Al}_2\text{O}_3/\text{AC}$  catalyst collected after the third run revealed the presence of  $\text{Ni}(\text{OH})_2$  species on the Ni surface (2p<sub>3/2</sub> and 2p<sub>1/2</sub> peaks at 855.9 and 862.5 eV, respectively, Fig. 5d) [47,48]. Similarly, the peaks associated with  $\text{Ni}^{2+}$  (67.0 eV) in the XPS profile of the passivated  $\text{Ni}_2 @\text{Al}_2\text{O}_3/\text{AC}$  catalyst was upshifted to 69.3 eV in the XPS profile of the spent  $\text{Ni}_2 @\text{Al}_2\text{O}_3/\text{AC}$  catalyst (Fig. 5e), indicating the formation of  $\text{Ni}(\text{OH})_2$  [67]. Therefore, passivated NiO was converted into  $\text{Ni}(\text{OH})_2$  during the subcritical water reaction. The formation of  $\text{Ni}(\text{OH})_2$  can contribute to the decrease in catalytic activity of the  $\text{Ni}_2 @\text{Al}_2\text{O}_3/\text{AC}$  catalyst for the conversion of PRS into polyols and monocarboxylic acids. The crystallinity of the Ni NPs of the spent  $\text{Ni}_2 @\text{Al}_2\text{O}_3/\text{AC}$  catalyst collected after the third run was higher than that of the Ni NPs of the fresh  $\text{Ni}_2 @\text{Al}_2\text{O}_3/\text{AC}$  catalyst. This was ascribed to the agglomeration of neighboring Ni NPs during reactivation. The HR–TEM images of the catalysts collected after the third run were shown in Fig. S29. The non-magnetic solid consisted of the  $\text{Pd}_{0.1}/\text{CN}_x\text{-DP4}$  and  $\text{Ni}_2 @\text{Al}_2\text{O}_3/\text{AC}$  catalysts (Figs. S29a–c). Single Pd atom and Pd nanoclusters were observed in the spent  $\text{Pd}_{0.1}/\text{CN}_x\text{-DP4}$  catalyst (Fig. S29b). The Ni NPs of the spent  $\text{Ni}_2 @\text{Al}_2\text{O}_3/\text{AC}$  catalyst collected after the third run were agglomerated (Figs. S29d and e). The interparticle agglomeration did not decrease the PRS conversion and selectivities toward polyols and monocarboxylic acids during the third run, but had an effect on the selectivity during the extended runs (Fig. S28). Therefore, more in-depth research would be required to design highly-stable cellulose conversion catalyst for the total cascade conversion of birch wood into biochemicals.

#### 4. Conclusion

In summary, we demonstrated that the two-step cascade reaction of lignocellulosic biomass over the  $\text{Pd}_{0.1}/\text{CN}_x$  and  $\text{Ni}_2 @\text{Al}_2\text{O}_3/\text{AC}$  catalysts is a highly promising approach for producing high-yield LDPMs and LDDs, holocellulose-derived polyols, and monocarboxylic acids. The LDPM, LDD, PRS yields for the fractionation of birch wood in methanol at 250 °C and an initial  $\text{H}_2$  pressure of 3.0 MPa for 3 h over the  $\text{Pd}_{0.1}/\text{CN}_x\text{-DP4}$  catalyst were 11.1 wt%, 5.6%, and 63.4 wt% based on the total weight of glucans, xylans, and lignin, respectively; moreover, the PRS presented a high DOD of 84.6 wt%. The LDPM yield based on the amount of C in lignin, STY, and holocellulose retention were 53.6 C%, 1186.6 g<sub>LDPMs</sub> g<sub>Pd</sub><sup>−1</sup> h<sup>−1</sup>, and 79.6 wt%, respectively. The fractionation performance of the  $\text{Pd}_{0.1}/\text{CN}_x\text{-DP4}$ ,  $\text{Pd}_{0.1}/\text{CN}_x\text{-WI}$ , and  $\text{Pd}_{0.1}/\text{CN}_x\text{-CI4}$ , and  $\text{Pd}_{0.1}/\text{CN}_x\text{-CI8}$  catalysts were compared, and the results revealed that the numbers of atomically dispersed Pd of the catalysts played a critical role in stabilizing the reactive lignin intermediates. Upon reacting the PRS collected after fractionation in subcritical water at 270 °C and at an initial  $\text{H}_2$  pressure of 3.0 MPa for 1 h over the passivated  $\text{Ni}_2 @\text{Al}_2\text{O}_3/\text{AC}$  catalyst, an almost complete PRS conversion of 91.5 wt% with C<sub>2</sub>–C<sub>6</sub> polyol and monocarboxylic acid yields of 21.6 and 7.9 wt%, respectively were achieved. The total carbon yield of the holocellulose-derived polyols and monocarboxylic acids obtained from the PRS (51.1 C%) was similar to those of the cellulose-, glucose-, and fructose-derived products (46.1–59.6 C%). Using their different magnetic properties, the spent  $\text{Pd}_{0.1}/\text{CN}_x\text{-DP4}$  and passivated  $\text{Ni}_2 @\text{Al}_2\text{O}_3/\text{AC}$  catalyst were separated and reused three times with slight decreases in their fractionation and reaction activities (LDPM yield, 47.9 C%; polyol and monocarboxylic acid yield, 49.8 C%). Overall, we believe that the two-step cascade conversion method developed in this study is

highly promising in producing value-added platform chemicals directly from lignocellulosic biomass. This can be advantageous for developing cost-effective biorefineries.

### CRediT authorship contribution statement

**Jaeyong Park:** Conceptualization, Methodology, Formal analysis, Data curation, Writing – original draft. **Umair Mushtaq:** Conceptualization, Methodology, Investigation. **Junjung Rohmat Sugiarto:** Validation, Data curation, Visualization. **Deepak Verma:** Methodology, Formal analysis, Investigation. **Jaehoon Kim:** Supervision, Project administration, Resources, Writing – review & editing, Funding acquisition.

### Declaration of Competing Interest

The authors declare that they have no known competing financial interests or personal relationships that could have appeared to influence the work reported in this paper.

### Acknowledgements

This study was supported by the Technology Development Program to Solve Climate Change of the National Research Foundation (NRF), funded by the Ministry of Science, ICT & Future Planning (2020M1A2A2080430). Additional support from a National Research Foundation of Korea (NRF) grant funded by the Ministry of Science and ICT, Republic of Korea is also acknowledged (grant numbers 2020R1C1C1003236 and 2020H1D3A2A02085762). We used the 10 C synchrotron beamline of the Pohang Acceleration Laboratory (PAL, Korea) under contact no. 20211st-10C-037.

### Appendix A. Supporting information

Supplementary data associated with this article can be found in the online version at [doi:10.1016/j.apcatb.2022.121280](https://doi.org/10.1016/j.apcatb.2022.121280).

### References

- [1] Y. Liao, S.-F. Koelewijn, G. Van den Bossche, J. Van Aelst, S. Van den Bosch, T. Renders, K. Navare, T. Nicolai, K. Van Aelst, M. Maesen, A sustainable wood biorefinery for low-carbon footprint chemicals production, *Science* 367 (2020) 1385–1390, <https://doi.org/10.1126/science.aau1567>.
- [2] J. Pang, J. Sun, M. Zheng, H. Li, Y. Wang, T. Zhang, Transition metal carbide catalysts for biomass conversion: a review, *Appl. Catal. B* 254 (2019) 510–522, <https://doi.org/10.1016/j.apcatb.2019.05.034>.
- [3] M. Carrier, A. Loppinet-Serani, D. Denux, J.-M. Lasnier, F. Ham-Pichavant, F. Cansell, C. Aymonier, Thermogravimetric analysis as a new method to determine the lignocellulosic composition of biomass, *Biomass Bioenergy* 35 (2011) 298–307, <https://doi.org/10.1016/j.biombioe.2010.08.067>.
- [4] Y. Lu, Z. Zhang, H. Wang, Y. Wang, Toward efficient single-atom catalysts for renewable fuels and chemicals production from biomass and CO<sub>2</sub>, *Appl. Catal. B* 292 (2021), 120162, <https://doi.org/10.1016/j.apcatb.2021.120162>.
- [5] W. Schutyser, T. Renders, S. Van den Bosch, S.F. Koelewijn, G.T. Beckham, B. F. Sels, Chemicals from lignin: an interplay of lignocellulose fractionation, depolymerisation, and upgrading, *Chem. Soc. Rev.* 47 (2018) 852–908, <https://doi.org/10.1039/C7CS00566K>.
- [6] J. Zakzeski, P.C.A. Bruijninx, A.L. Jongerius, B.M. Weckhuysen, The catalytic valorization of lignin for the production of renewable chemicals, *Chem. Rev.* 110 (2010) 3552–3599, <https://doi.org/10.1021/cr900354u>.
- [7] W.M. Goldmann, J. Ahola, M. Mikola, J. Tanskanen, Formic acid aided hot water extraction of hemicellulose from European silver birch (*Betula pendula*) sawdust, *Bioresour. Technol.* 232 (2017) 176–182, <https://doi.org/10.1016/j.biortech.2017.02.032>.
- [8] B. Op de Beeck, M. Dusselier, J. Geboers, J. Holsbeek, E. Morré, S. Oswald, L. Giebler, B.F. Sels, Direct catalytic conversion of cellulose to liquid straight-chain alkanes, *Energy Environ. Sci.* 8 (2015) 230–240, <https://doi.org/10.1039/C4EE01523A>.
- [9] Y. Liu, L. Chen, T. Wang, Q. Zhang, C. Wang, J. Yan, L. Ma, One-pot catalytic conversion of raw lignocellulosic biomass into gasoline alkanes and chemicals over LiTaMoO<sub>6</sub> and Ru/C in aqueous phosphoric acid, *ACS Sustain. Chem. Eng.* 3 (2015) 1745–1755, <https://doi.org/10.1021/acssuschemeng.5b00256>.
- [10] Q. Xia, Z. Chen, Y. Shao, X. Gong, H. Wang, X. Liu, S.F. Parker, X. Han, S. Yang, Y. Wang, Direct hydrodeoxygenation of raw woody biomass into liquid alkanes, *Nat. Commun.* 7 (2016) 11162, <https://doi.org/10.1038/ncomms11162>.
- [11] C. Li, M. Zheng, A. Wang, T. Zhang, One-pot catalytic hydrocracking of raw woody biomass into chemicals over supported carbide catalysts: simultaneous conversion of cellulose, hemicellulose and lignin, *Energy Environ. Sci.* 5 (2012) 6383–6390, <https://doi.org/10.1039/C1EE02684D>.
- [12] T.D. Matson, K. Barta, A.V. Iretskii, P.C. Ford, One-pot catalytic conversion of cellulose and of woody biomass solids to liquid fuels, *J. Am. Chem. Soc.* 133 (2011) 14090–14097, <https://doi.org/10.1021/ja205436c>.
- [13] A.W. Bartling, M.L. Stone, R.J. Hanes, A. Bhatt, Y. Zhang, M.J. Bidy, R. Davis, J. S. Kruger, N.E. Thornburg, J.S. Luterbacher, R. Rinaldi, J.S.M. Samec, B.F. Sels, Y. Román-Leshkov, G.T. Beckham, Techno-economic analysis and life cycle assessment of a biorefinery utilizing reductive catalytic fractionation, *Energy Environ. Sci.* 14 (2021) 4147–4168, <https://doi.org/10.1039/D1EE01642C>.
- [14] M.M. Abu-Omar, K. Barta, G.T. Beckham, J.S. Luterbacher, J. Ralph, R. Rinaldi, Y. Román-Leshkov, J.S.M. Samec, B.F. Sels, F. Wang, Guidelines for performing lignin-first biorefining, *Energy Environ. Sci.* 14 (2021) 262–292, <https://doi.org/10.1039/D0EE02870C>.
- [15] S. Van den Bosch, W. Schutyser, R. Vanholme, T. Driessen, S.F. Koelewijn, T. Renders, B. De Meester, W.J.J. Huijgen, W. Dehaen, C.M. Courtin, B. Lagrain, W. Boerjan, B.F. Sels, Reductive lignocellulose fractionation into soluble lignin-derived phenolic monomers and dimers and processable carbohydrate pulps, *Energy Environ. Sci.* 8 (2015) 1748–1763, <https://doi.org/10.1039/C5EE00204D>.
- [16] Q. Song, F. Wang, J. Cai, Y. Wang, J. Zhang, W. Yu, J. Xu, Lignin depolymerization (LDP) in alcohol over nickel-based catalysts via a fragmentation-hydrogenolysis process, *Energy Environ. Sci.* 6 (2013) 994–1007, <https://doi.org/10.1039/C2EE23741E>.
- [17] S. Van den Bosch, T. Renders, S. Kennis, S.F. Koelewijn, G. Van den Bossche, T. Vangeel, A. Deneyer, D. Depuydt, C.M. Courtin, J.M. Thevelein, W. Schutyser, B. F. Sels, Integrating lignin valorization and bio-ethanol production: on the role of Ni-Al<sub>2</sub>O<sub>3</sub> catalyst pellets during lignin-first fractionation, *Green. Chem.* 19 (2017) 3313–3326, <https://doi.org/10.1039/C7GC01324H>.
- [18] A. Deneyer, E. Peeters, T. Renders, S. Van den Bosch, N. Van Oeckel, T. Ennaert, T. Szarvas, T.I. Korányi, M. Dusselier, B.F. Sels, Direct upstream integration of biogasoline production into current light straight run naphtha petrorefinery processes, *Nat. Energy* 3 (2018) 969–977, <https://doi.org/10.1038/s41560-018-0245-6>.
- [19] Z. Sun, G. Bottari, A. Afanasenko, M.C.A. Stuart, P.J. Deuss, B. Fridrich, K. Barta, Complete lignocellulose conversion with integrated catalyst recycling yielding valuable aromatics and fuels, *Nat. Catal.* 1 (2018) 82–92, <https://doi.org/10.1038/s41929-017-0007-z>.
- [20] N. Díez, R. Mysyk, W. Zhang, E. Goikolea, D. Carriazo, One-pot synthesis of highly activated carbons from melamine and terephthalaldehyde as electrodes for high energy aqueous supercapacitors, *J. Mater., Chem. A* 5 (2017) 14619–14629, <https://doi.org/10.1039/C7TA01424D>.
- [21] J. Park, H.S. Cahyadi, U. Mushtaq, D. Verma, D. Han, K.-W. Nam, S.K. Kwak, J. Kim, Highly efficient reductive catalytic fractionation of lignocellulosic biomass over extremely low-loaded Pd catalysts, *ACS Catal.* 10 (2020) 12487–12506, <https://doi.org/10.1021/acscatal.0c03393>.
- [22] K. Van Aelst, E. Van Sinay, T. Vangeel, E. Cooreman, G. Van den Bossche, T. Renders, J. Van Aelst, S. Van den Bosch, B.F. Sels, Reductive catalytic fractionation of pine wood: elucidating and quantifying the molecular structures in the lignin oil, *Chem. Sci.* 11 (2020) 11498–11508, <https://doi.org/10.1039/D0SC04182C>.
- [23] R.F. Susanti, L.W. Dianngrum, T. Yum, Y. Kim, B.G. Lee, J. Kim, High-yield hydrogen production from glucose by supercritical water gasification without added catalyst, *Int. J. Hydrog. Energy* 37 (2012) 11677–11690, <https://doi.org/10.1016/j.ijhydene.2012.05.087>.
- [24] J. Zhang, L. Lombardo, G. Gözaydın, P.J. Dyson, N. Yan, Single-step conversion of lignin monomers to phenol: Bridging the gap between lignin and high-value chemicals, *Chin. J. Catal.* 39 (2018) 1445–1452, [https://doi.org/10.1016/S1872-2067\(18\)63132-8](https://doi.org/10.1016/S1872-2067(18)63132-8).
- [25] L. Li, L. Dong, X. Liu, Y. Guo, Y. Wang, Selective production of ethylbenzene from lignin oil over FeOx modified Ru/Nb<sub>2</sub>O<sub>5</sub> catalyst, *Appl. Catal. B* 260 (2020), 118143, <https://doi.org/10.1016/j.apcatb.2019.118143>.
- [26] S. Song, J. Zhang, G. Gözaydın, N. Yan, Production of terephthalic acid from corn stover lignin, *Angew. Chem., Int. Ed.* 58 (2019) 4934–4937, <https://doi.org/10.1002/anie.201814284>.
- [27] D. Verma, R. Insyani, H.S. Cahyadi, J. Park, S.M. Kim, J.M. Cho, J.W. Bae, J. Kim, Ga-doped Cu/H-nanozeolite-Y catalyst for selective hydrogenation and hydrodeoxygenation of lignin-derived chemicals, *Green. Chem.* 20 (2018) 3253–3270, <https://doi.org/10.1039/C8GC00629F>.
- [28] V. Ranaware, D. Verma, R. Insyani, A. Riaz, S.M. Kim, J. Kim, Highly-efficient and magnetically-separable ZnO/Co@N-CNTs catalyst for hydrodeoxygenation of lignin and its derived species under mild conditions, *Green. Chem.* 21 (2019) 1021–1042, <https://doi.org/10.1039/C8GC03623C>.
- [29] Z. Sun, B. Fridrich, A. de Santi, S. Elangovan, K. Barta, Bright side of lignin depolymerization: toward new platform chemicals, *Chem. Rev.* 118 (2018) 614–678, <https://doi.org/10.1021/acs.chemrev.7b00588>.
- [30] Y. Huang, Y. Duan, S. Qiu, M. Wang, C. Ju, H. Cao, Y. Fang, T. Tan, Lignin-first biorefinery: a reusable catalyst for lignin depolymerization and application of lignin oil to jet fuel aromatics and polyurethane feedstock, *Sustain. Energy Fuels* 2 (2018) 637–647, <https://doi.org/10.1039/C7SE00535K>.
- [31] Z. Cao, M. Dierks, M.T. Clough, I.B. Dalto de Castro, R. Rinaldi, A convergent approach for a deep converting lignin-first biorefinery rendering high-energy-

- density drop-in fuels, *Joule* 2 (2018) 1118–1133, <https://doi.org/10.1016/j.joule.2018.03.012>.
- [32] M. Zheng, J. Pang, R. Sun, A. Wang, T. Zhang, Selectivity control for cellulose to diols: dancing on eggs, *ACS Catal.* 7 (2017) 1939–1954, <https://doi.org/10.1021/acscatal.6b03469>.
- [33] J. Moncada, C.A. Cardona, L.E. Rincón, Design and analysis of a second and third generation biorefinery: the case of castorbean and microalgae, *Bioresour. Technol.* 198 (2015) 836–843, <https://doi.org/10.1016/j.biortech.2015.09.077>.
- [34] R.X. Jiménez, A.F. Young, H.L.S. Fernandes, Propylene glycol from glycerol: process evaluation and break-even price determination, *Renew. Energy* 158 (2020) 181–191, <https://doi.org/10.1016/j.renene.2020.05.126>.
- [35] I. Baumann, P. Westermann, Microbial production of short chain fatty acids from lignocellulosic biomass: current processes and market, *BioMed. Res. Int.* 2016 (2016) 8469357, <https://doi.org/10.1155/2016/8469357>.
- [36] C. Le Berre, P. Serp, P. Kalck, G.P. Torrence, *Acetic Acid*, *Ullmann's Encyclopedia of Industrial Chemistry*, 2000, pp. 1–34, [https://doi.org/10.1002/14356007.a01\\_045.pub3](https://doi.org/10.1002/14356007.a01_045.pub3).
- [37] U.-R. Samel, W. Kohler, A.O. Gamer, U. Keuser, S.-T. Yang, Y. Jin, M. Lin, Z. Wang, J.H. Teles, *Propionic Acid and Derivatives*, *Ullmann's Encyclopedia of Industrial Chemistry*, 2000, pp. 1–20, [https://doi.org/10.1002/14356007.a22\\_223.pub4](https://doi.org/10.1002/14356007.a22_223.pub4).
- [38] M. Dwidar, J.-Y. Park, R.J. Mitchell, B.-I. Sang, The future of butyric acid in industry, *Sci. World J.* 2012 (2012), 471417, <https://doi.org/10.1100/2012/471417>.
- [39] S. Van den Bosch, W. Schutyser, S.F. Koelewijn, T. Renders, C.M. Courtin, B.F. Sels, Tuning the lignin oil OH-content with Ru and Pd catalysts during lignin hydrogenolysis on birch wood, *Chem. Commun.* 51 (2015) 13158–13161, <https://doi.org/10.1039/C5CC04025F>.
- [40] X. Ouyang, X. Huang, J. Zhu, M.D. Boot, E.J.M. Hensen, Catalytic conversion of lignin in woody biomass into phenolic monomers in methanol/water mixtures without external hydrogen, *ACS Sustain. Chem. Eng.* 7 (2019) 13764–13773, <https://doi.org/10.1021/acssuschemeng.9b01497>.
- [41] I. Klein, C. Marcum, H. Kenttämä, M.M. Abu-Omar, Mechanistic investigation of the Zn/Pd/C catalyzed cleavage and hydrodeoxygenation of lignin, *Green. Chem.* 18 (2016) 2399–2405, <https://doi.org/10.1039/C5GC01325A>.
- [42] X. Huang, J. Zhu, T.I. Korányi, M.D. Boot, E.J.M. Hensen, Effective release of lignin fragments from lignocellulose by Lewis acid metal triflates in the lignin-first approach, *ChemSusChem* 9 (2016) 3262–3267, <https://doi.org/10.1002/cssc.201601252>.
- [43] W. Liu, Y. Chen, H. Qi, L. Zhang, W. Yan, X. Liu, X. Yang, S. Miao, W. Wang, C. Liu, A. Wang, J. Li, T. Zhang, A durable nickel single-atom catalyst for hydrogenation reactions and cellulose valorization under harsh conditions, *Angew. Chem., Int. Ed.* 57 (2018) 7071–7075, <https://doi.org/10.1002/anie.201802231>.
- [44] L. Kuai, Z. Chen, S. Liu, E. Kan, N. Yu, Y. Ren, C. Fang, X. Li, Y. Li, B. Geng, Titania supported synergistic palladium single atoms and nanoparticles for room temperature ketone and aldehydes hydrogenation, *Nat. Commun.* 11 (2020) 48, <https://doi.org/10.1038/s41467-019-13941-5>.
- [45] J. Park, A. Riaz, D. Verma, H.J. Lee, H.M. Woo, J. Kim, Fractionation of lignocellulosic biomass over core-shell Ni@Al<sub>2</sub>O<sub>3</sub> catalysts with formic acid as a cocatalyst and hydrogen source, *ChemSusChem* 12 (2019) 1743–1762, <https://doi.org/10.1002/cssc.201802847>.
- [46] P. Ferrini, R. Rinaldi, Catalytic biorefining of plant biomass to non-pyrolytic lignin bio-oil and carbohydrates through hydrogen transfer reactions, *Angew. Chem., Int. Ed.* 53 (2014) 8634–8639, <https://doi.org/10.1002/anie.201403747>.
- [47] A.P. Grosvenor, M.C. Biesinger, R.S.C. Smart, N.S. McIntyre, New interpretations of XPS spectra of nickel metal and oxides, *Surf. Sci.* 600 (2006) 1771–1779, <https://doi.org/10.1016/j.susc.2006.01.041>.
- [48] A. Sápi, G. Halasi, J. Kiss, D.G. Dobó, K.L. Juhász, V.J. Kolcsár, Z. Ferencz, G. Vári, V. Matolin, A. Erdőhelyi, A. Kukovecz, Z. Kónya, In Situ DRIFTS and NAP-XPS exploration of the complexity of CO<sub>2</sub> hydrogenation over size-controlled Pt nanoparticles supported on mesoporous NiO, *J. Phys. Chem. C* 122 (2018) 5553–5565, <https://doi.org/10.1021/acs.jpcc.8b00061>.
- [49] L. Segal, J.J. Creely, A.E. Martin, C.M. Conrad, An empirical method for estimating the degree of crystallinity of native cellulose Using the X-ray diffractometer, *Text. Res. J.* 29 (1959) 786–794, <https://doi.org/10.1177/004051755902901003>.
- [50] R. Muangrat, J.A. Onwudili, P.T. Williams, Influence of NaOH, Ni/Al<sub>2</sub>O<sub>3</sub> and Ni/SiO<sub>2</sub> catalysts on hydrogen production from the subcritical water gasification of model food waste compounds, *Appl. Catal., B* 100 (2010) 143–156, <https://doi.org/10.1016/j.apcatb.2010.07.024>.
- [51] C. Liu, C. Zhang, S. Sun, K. Liu, S. Hao, J. Xu, Y. Zhu, Y. Li, Effect of WOX on bifunctional Pd-WOX/Al<sub>2</sub>O<sub>3</sub> catalysts for the selective hydrogenolysis of glucose to 1,2-propanediol, *ACS Catal.* 5 (2015) 4612–4623, <https://doi.org/10.1021/acscatal.5b00800>.
- [52] A.A. Peterson, F. Vogel, R.P. Lachance, M. Fröling, J.M.J. Antal, J.W. Tester, Thermochemical biofuel production in hydrothermal media: A review of sub- and supercritical water technologies, *Energy Environ. Sci.* 1 (2008) 32–65, <https://doi.org/10.1039/B810100K>.
- [53] M. Uematsu, E.U. Frank, Static dielectric constant of water and steam, *J. Phys. Chem. Ref. Data* 9 (1980) 1291–1306, <https://doi.org/10.1063/1.555632>.
- [54] W.L. Marshall, E.U. Franck, Ion product of water substance, 0–1000 °C, 1–10,000 bars new international formulation and its background, *J. Phys. Chem. Ref. Data* 10 (1981) 295–304, <https://doi.org/10.1063/1.555643>.
- [55] R. Hausser, G. Maier, F. Noack, Kernmagnetische messungen von selbstdiffusions-Koeffizienten in Wasser und Benzol bis zum kritischen Punkt, *Z. für Naturforsch. A* 21 (1966) 1410–1415, <https://doi.org/10.1515/zna-1966-0914>.
- [56] X. Wang, L. Meng, F. Wu, Y. Jiang, L. Wang, X. Mu, Efficient conversion of microcrystalline cellulose to 1,2-alkanediols over supported Ni catalysts, *Green. Chem.* 14 (2012) 758–765, <https://doi.org/10.1039/C2GC15946E>.
- [57] R. Ooms, M. Dusselier, J.A. Geboers, B. Op de Beeck, R. Verhaeven, E. Gobechiya, J.A. Martens, A. Redl, B.F. Sels, Conversion of sugars to ethylene glycol with nickel tungsten carbide in a fed-batch reactor: high productivity and reaction network elucidation, *Green. Chem.* 16 (2014) 695–707, <https://doi.org/10.1039/C3GC41431K>.
- [58] B. Kusserow, S. Schimpf, P. Claus, Hydrogenation of glucose to sorbitol over nickel and ruthenium catalysts, *Adv. Synth. Catal.* 345 (2003) 289–299, <https://doi.org/10.1002/adsc.200390024>.
- [59] H. Schiweck, A. Bär, R. Vogel, E. Schwarz, M. Kunz, C. Dusaudois, A. Clement, C. Lefranc, B. Lüssem, M. Moser, S. Peters, Sugar Alcohols, *Ullmann's Encyclopedia of Industrial Chemistry*, [https://doi.org/10.1002/14356007.a25\\_413.pub3](https://doi.org/10.1002/14356007.a25_413.pub3).
- [60] N. Li, G.W. Huber, Aqueous-phase hydrodeoxygenation of sorbitol with Pt/SiO<sub>2</sub>-Al<sub>2</sub>O<sub>3</sub>: identification of reaction intermediates, *J. Catal.* 270 (2010) 48–59, <https://doi.org/10.1016/j.jcat.2009.12.006>.
- [61] Y. Kanie, K. Akiyama, M. Iwamoto, Reaction pathways of glucose and fructose on Pt nanoparticles in subcritical water under a hydrogen atmosphere, *Catal. Today* 178 (2011) 58–63, <https://doi.org/10.1016/j.cattod.2011.07.031>.
- [62] Z. Huo, J. Xiao, D. Ren, F. Jin, T. Wang, G. Yao, Chemoselective synthesis of propionic acid from biomass and lactic acid over a cobalt catalyst in aqueous media, *Green. Chem.* 19 (2017) 1308–1314, <https://doi.org/10.1039/C6GC03036J>.
- [63] Y. Wang, F. Jin, M. Sasaki, F. Wahyudiono, Z. Wang, M. Jing, Goto, Selective conversion of glucose into lactic acid and acetic acid with copper oxide under hydrothermal conditions, *AIChE J.* 59 (2013) 2096–2104, <https://doi.org/10.1002/aic.13960>.
- [64] N. Karanwal, D. Verma, P. Butolia, S.M. Kim, J. Kim, One-pot direct conversion of levulinic acid into high-yield valeric acid over a highly stable bimetallic Nb-Cu/Zr-doped porous silica catalyst, *Green. Chem.* 22 (2020) 766–787, <https://doi.org/10.1039/C9GC03516H>.
- [65] V.K. Velisoju, N. Gutta, J. Tardio, S.K. Bhargava, K. Vankudoth, A. Chatla, S. Medak, V. Akula, Hydrodeoxygenation activity of W modified Ni/H-ZSM-5 catalyst for single step conversion of levulinic acid to pentanoic acid: an insight on the reaction mechanism and structure activity relationship, *Appl. Catal., A* 550 (2018) 142–150, <https://doi.org/10.1016/j.apcata.2017.11.008>.
- [66] W.-C. Wen, S.C. Eady, L.T. Thompson, Oxide supported metal catalysts for the aldehyde water shift reaction: elucidating roles of the admetal, support, and synergies, *Catal. Today* 355 (2020) 199–204, <https://doi.org/10.1016/j.cattod.2019.03.064>.
- [67] A.M. Tarditi, N. Barroso, A.E. Galetti, L.A. Arrúa, L. Cornaglia, M.C. Abello, XPS study of the surface properties and Ni particle size determination of Ni-supported catalysts, *Surf. Interface Anal.* 46 (2014) 521–529, <https://doi.org/10.1002/sia.5549>.